The Hydrometeorology of Kuwait: Characterization and Modeling of Rainfall Distribution

by

Marc Pace Marcella

B.S., Cornell University (2005)

Submitted to the Department of Civil and Environmental Engineering
in partial fulfillment of the requirements for the degree of

Master of Science in Civil and Environmental Engineering

at the

MASSACHUSETTS INSTITUTE OF TECHNOLOGY

February 2008

Author .....
Department of Civil and Environmental Engineering
December 18, 2007

Certified by .....
Elfatih A.B. Eltahir
Professor of Civil and Environmental Engineering
Thesis Supervisor

Accepted by .....
Daniele Veneziano
Chairman, Departmental Committee for Graduate Students

The Hydrometeorology of Kuwait: Characterization and Modeling of Rainfall Distribution

by

Marc Pace Marcella

Submitted to the Department of Civil and Environmental Engineering
on December 18, 2007, in partial fulfillment of the
requirements for the degree of
Master of Science in Civil and Environmental Engineering

Abstract

This thesis presents a comprehensive study on the hydrometeorology of Kuwait. The spatial, seasonal, and interannual variability of Kuwait rainfall is discussed based on rain gauge and satellite datasets. It is found that the spatial distribution of Kuwait's annual rainfall features a gradual increase from the southwest to the northeast. Furthermore, Kuwait experiences a distinct rainy season from November to April, with double peaks in January and March. The seasonal variability of rainfall is associated with shifts in the pattern of mid-latitude storm tracks migrating towards the Middle East during the winter and spring seasons. These patterns are characterized using estimates of the spatial correlations of rainfall in Kuwait with the surrounding region. At the interannual timescale, significant correlation is found between the tropical El Niño-Southern Oscillation and annual rainfall anomalies. Similar correlations are found between mid-latitude rainfall in Europe and rainfall in Kuwait.

In addition, a new sub-cloud layer evaporation scheme is incorporated into Regional Climate Model 3 to better simulate the rainfall distribution over Kuwait. The new scheme represents sub-cloud layer evaporation of convective as well as large scale rainfall. These simulations show significant response to the incorporation of sub-cloud layer evaporation where a reduction of nearly 20% in annual rainfall occurs over the region. As a result, the new model simulations of annual rainfall are within 15% of observations. Results also indicate that the interannual variability of rainfall simulated by RegCM3 is sensitive to the specification of boundary conditions. Moreover, with sub-cloud layer evaporation incorporated as well as ERA40 boundary conditions implemented, the model's bias and root mean square error are significantly reduced. Therefore, the model's ability to reproduce observed annual rainfall and the yearly variations of rainfall is greatly improved. Ultimately, the analysis presented here allows for the future assessment of climate variability of Kuwait.

Thesis Supervisor: Elfatih A.B. Eltahir
Title: Professor of Civil and Environmental Engineering

Acknowledgments

First, I thank my advisor, Elfatih Eltahir, for all his help, knowledge, and guidance in my research and academic ventures here at the Institute. From words of encouragement to words of critique, without his presence the work provided here would simply not be possible—I thank Fatih for the opportunity and attribute much of my graduate success to his unwavering support. Whether it be hours spent in classrooms or times tucked away in Room 305, I have learned more in the past two years than I ever thought possible. Next, Jonathan Winter. Be it Fortran coding or the nuances of RegCM3, without his help, patience, and at times perseverance (for the both of us), most of what I have accomplished here would be rather lackluster. I'd also like to acknowledge the rest of the Eltahir research group especially Arne Bomblies, Gayle Sherman, and Rebecca Gianotti. Expanding upon the M.I.T. community to some members of Parsons Lab, namely, Frederic Chagnon, Ryan Knox, Gautaum Bisht, and Lejo Flores, thank you guys for fielding my questions and respecting my absentmindedness. Spanning even further out (internationally), I thank Jeremy Pal, the ICTP community, and specifically Moetasim, who without their help I may still not be looking at some model results. Also, I express my gratitude to two of the most important professors of my undergraduate career: Arthur DeGaetano and Mark Wysocki....may the memories of the Chapter House live on.

Likewise, I thank and owe much to many of my close friends. Of those not mentioned above but definitely of noteworthiness are Delavan Dickson, Alicia McNeil, Kristen Giosmas, Kacie Lally, Tommy Mahoney, Jackey West, and Phil Lane. From roommates and classmates, to shoulders and ears, to sometimes even the occasional openhanded "greeting" each one of you has had your own little hand in the success I have been too lucky to have had.

Lastly and most importantly, I thank my family. Without their comfort, support, and unconditional love, I wouldn't be the person I am, where I am, today. First, my parents. To my mom who has pushed me since kindergarten and loved me since birth, I thank you for being you—someone I am proud to call my mother. My dad, who has played therapist, financial supporter, and most importantly best friend...thank you for always being there.

And finally to my sister—confidant and loyal friend—thank you for being the wonderful person you are.

Funding for this research has been provided by the Kuwait Foundation for the Advancement of Science and the Linden Fellowship.

Contents

List of Figures

List of Tables

Chapter 1

Introduction

1.1 Motivation

With low annual rainfall and long, hot, summers, the scarcity of water resources has long plagued the Middle East [Rogers and Lydon, 1994]. Surrounded by the Syrian and Arabian Deserts to the west and the Persian Gulf to the east, the country of Kuwait is centrally located in this arid region (Figure 1-1). Due to few natural freshwater sources itself, Kuwait's situation is particularly difficult. Within the last three decades, the nation's population has nearly doubled while domestic water demand has nearly tripled [Fadlelmawla and Al-Otaibi, 2005]. Recent reports indicate that Kuwaiti domestic water consumption now totals over 400 $L\ day^{-1}$ per capita [Al-Rashed and Sherif, 2000]. Further work has shown that the pattern of water consumption in the country is well correlated with atmospheric conditions such as temperature, relative humidity, and rainfall as shown in Figure 1-2 [Mukhopadhyay *et al.*, 2000]. In sharp contrast, extreme rainfall events, where more than 10 cm of rain falls in just a few hours, can result in large surface runoff and property damage for urban areas of the country [Al-Rashed and Sherif, 2000]. Therefore, it is necessary to understand fully the spatial and temporal distribution of rainfall in the country. To this date, little work has been done on describing or modeling the rainfall distribution of the nation.

As mentioned, the combination of short, distinct, rainy seasons and limited renewable freshwater resources are important motivations for studying rainfall variability in the Mid-

Figure 1-1: NASA Shuttle Radar Topography Mission (SRTM) and Moderate Resolution Imaging Spectroradiometer (MODIS) image from 2000 of the Middle East from the California Geographical Survey. Highlighted in red is Kuwait.

dle East and in particular Kuwait. For example, Egypt, Kuwait, and Bahrain, all consume more than 2000% of their natural freshwater resources (Figure 1-3) [Human Rights Development Report, 2000]. Here a comprehensive record and detailed rainfall history that includes traditional land measurements as well as novel satellite observations is compiled for Kuwait. From this collection, a description of the country's rainfall variability is produced. Walters [1988] provides a thorough description of circulation patterns of the Middle East but mentions neither Kuwait's rainfall nor climate in detail. In contrast, Al Kulaib [1984] describes the major climatic characteristics of the country but does not compile a complete rainfall record. Hence, for any future climate analysis or modeling, a reliable rainfall climatology should be constructed. Succinctly, with rain gauge and satellite measurements,

this study aims to quantify in detail Kuwait's rainfall record. Lastly, attempting to explain variability of Kuwait rainfall, these datasets are used to also test for correlations between Kuwait rainfall and other large scale atmospheric circulation patterns. As a result, these findings should ultimately explain some of the rainfall variability in Kuwait.

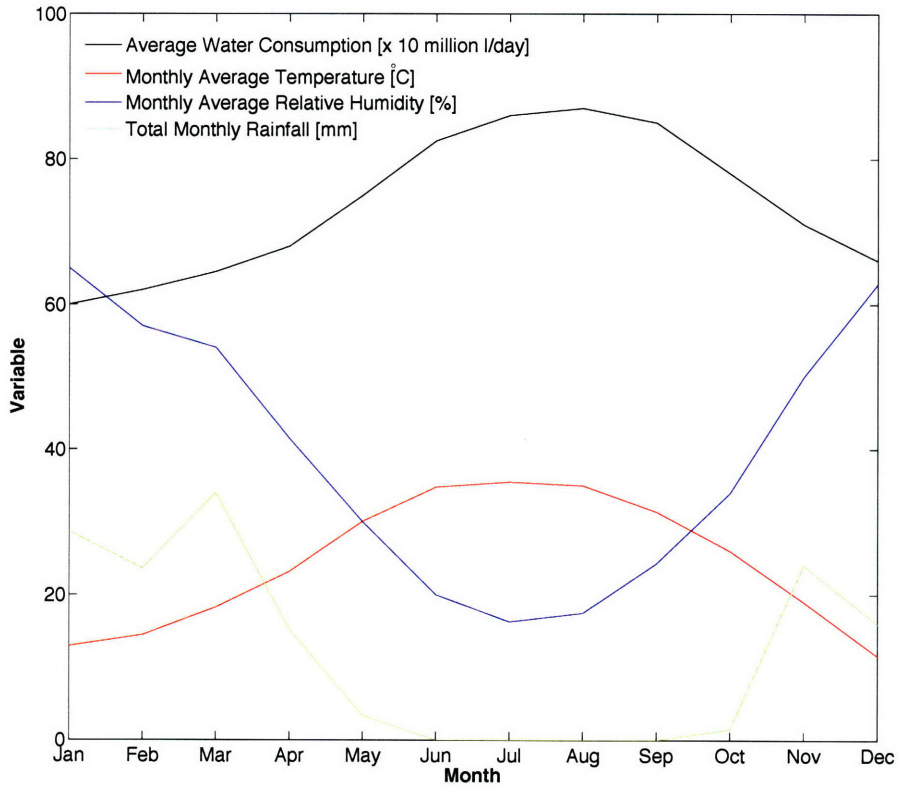

Figure 1-2: Kuwait average monthly water consumption with corresponding atmospheric conditions for the period of 1992-1998, Mukhopadhyay *et al.* [2000].

Furthermore, to allow for the future assessment of climate variability of Kuwait, we present a modified regional climate model (RCM) that more accurately simulates rainfall over semi-arid regions. Prior studies have indicated that the neglect of sub-cloud rainfall evaporation in a RCM leads to an overestimation of rainfall in semi-arid climates [Small *et al.*, 1999]. In a recent paper, Evans *et al.* [2004] use a RCM to study rainfall processes over the Middle East. Although their results show an overestimation of rainfall in Saudi Arabia and the Persian Gulf region, they do not address the cause of this bias. Re-

cently, Worden *et al.* [2007] reaffirm the significance of raindrop evaporation, reporting that nearly 20% (to as much as 50%) of rainfall evaporates near convective clouds over the tropics. Here, a more physically realistic representation of sub-cloud layer evaporation is incorporated in a regional climate model. In addition, the sensitivity of RegCM3 to lateral boundary conditions in simulating Kuwait's rainfall distribution is examined. A comparison of simulation results to a variety of observational datasets is completed to determine the effects of subcloud layer evaporation and lateral boundary conditions on simulating Kuwait's rainfall. Ultimately, this work leads to a better description, simulation, as well as prediction of the rainfall distribution over Kuwait and the surrounding region.

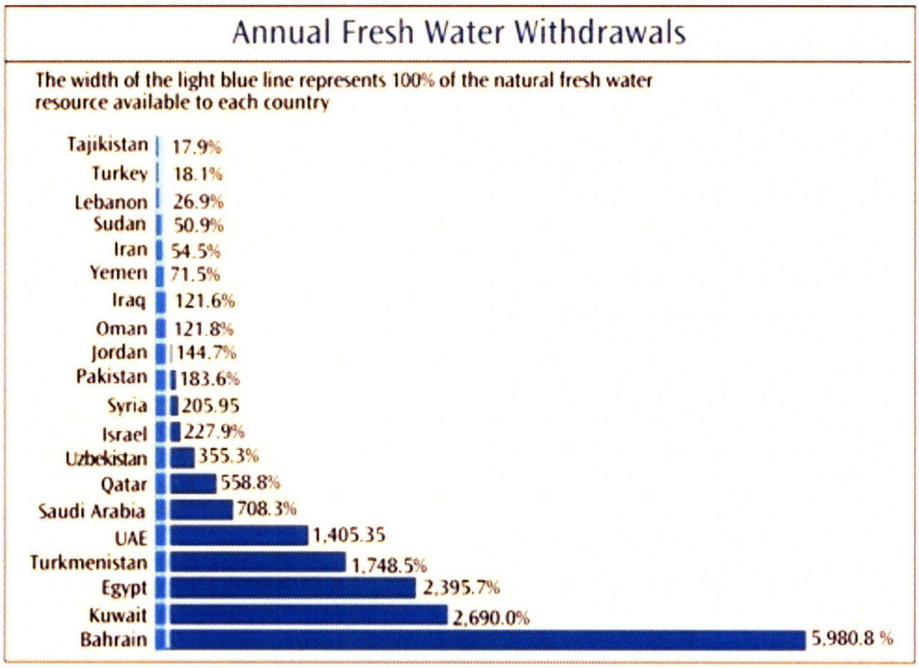

Figure 1-3: Human Rights Development Report [2000] figure highlighting the stress on Freshwater resources for Middle East countries. Dark blue bars indicate the actual freshwater withdrawn compared to what is naturally available (in percentage,) whereas light blue bars indicate 100% of the natural freshwater resources available for each country.

Chapter 2

Hydroclimatology of Kuwait

The following chapter describes the hydroclimatology of Kuwait. Currently, little work has been completed in compiling a robust record of rainfall in the country. In addition to a broad overview of the hydroclimatology, efforts are made to explain the variability of rainfall experienced in Kuwait at the seasonal and interannual timescales.

2.1 Observational Datasets

From the Tropical Rainfall Measurement Mission (TRMM) to NCEP reanalysis data, a variety of rainfall datasets were considered in this study. However, the country of Kuwait spans a small area from 28.4°N to 30.2°N, and 46.5°E to 48.5°E. Therefore, datasets with a long historical record as well as high spatial resolution are desired. As a result, the three datasets below were used in the analysis. Table 2.1 provides a summary of the temporal coverage for each dataset.

2.1.1 Climate Research Unit High Resolution Gridded Dataset TS 2.1 (CRU)

The CRU fine resolution gridded dataset, TS 2.1, consists of a monthly time series of various climate variables covering the period 1900 to 2002. Such variables include surface temperature, precipitation, and vapor pressure—all interpolated from surface observations

onto a global 0.5° x 0.5° resolution grid [Mitchell and Jones, 2005]. The goal of the CRU database is to provide the best estimate of the spatial pattern of climate variables [New *et al.*, 1999]. Many studies [e.g., Yiao and Caya [2006] and Syed *et al.* [2006]] have used the CRU rainfall dataset for climate analysis and model validation. The weight placed on each station for a given gridbox is a function of the station's distance from the gridbox assuming an exponential correlation decay distance (450 km correlation scale for precipitation). If there is insufficient data for a gridbox, the 1960-1990 average value is used. The exact construction and description of the interpolation scheme used for each variable can be found in Mitchell and Jones [2005]. The CRU data available for the past fifty years (1952-2002) is used in this study.

2.1.2 Global Precipitation Climatology Project (GPCP)

Established in 1979 by the World Climate Research Program (WCRP), the Global Precipitation Climatology Project (GPCP), combines satellite observations and rain gauge measurements to produce precipitation estimates. Satellite measurements are computed from the Special Sensor Microwave/Imager (SSM/I) as well as the Atmospheric Infrared Sounder (AIRS) [Adler *et al.*, 2003]. Estimates obtained from the SSM/I and AIRS are then merged with rain gauge data, which is collected and maintained by the Global Precipitation Climatology Centre (GPCC). The output is a monthly, global, total precipitation product of 2.5° x 2.5° resolution from 1979 to present. It is important to note that no single satellite data source encompasses the entire GPCP record. In fact, four distinct periods exist in which data coverage changed including the incorporation of SSM/I data in 1987.

2.1.3 Kuwait International Airport Rain Gauge (WMO)

Lastly, located at 29.13°N, 47.58°E in Kuwait City, the Kuwait International Airport rain gauge data is also used for analysis. The airport has kept a nearly continuous record of monthly mean temperature, pressure, and total precipitation. Through the World Meteorological Organization (WMO) and the World Weather Records (WWR) compilation, these measurements are readily available from 1961 to present. Other station data exists within

	CRU	GPCP	WMO
Temporal Coverage	1952-2002	1979-2004	1961-2002
Spatial Coverage	Land Only	Global	Kuwait City
Resolution	0.5° x 0.5°	2.5° x 2.5°	—
Measurement Type	Gauge Interpolation	Satellite/Gauge	Gauge

Table 2.1: Summary of observation datasets surveyed in this study.

Kuwait, but none with such a substantial continuity in their observations. The airport station data along with CRU and GPCP data will be compared to simulations of monthly, annual, and interannual variability of rainfall in Kuwait.

2.2 Rainfall Statistics and Variability

2.2.1 Spatial Variability of Annual Rainfall

Shown in Figure 2-1 is the spatial distribution of rainfall over the Middle East for both CRU and GPCP datasets. From the wetter regions in the north of the Black and Caspian Seas to the drier areas in the south of the Syrian Desert and Arabian Peninsula, the gradient in Middle East precipitation is clear in both CRU and GPCP datasets. Interestingly, the effects of orographic lifting from the Zagros Mountains of western Iran are clearly seen where there is a a northeast increase in precipitation from Kuwait to Iraq in the north in Iraq and easterly into Iran. Although this pattern is noticeable in both the CRU and GPCP datasets, it is more apparent in CRU data over Kuwait (Figure 2-2). Here, nearly a doubling of annual rainfall (from 90mm to 180mm) occurs from the southwest, bordering Saudi Arabia, to the northeast, near coastal southern Iran. Moreover, it appears that coastal areas of Kuwait exhibit higher annual totals than interior regions (see Figure 2-2). For example, rainfall totals increase from 100 mm in the west to nearly 140 mm near Bubiyan and the Failaka Islands of the Persian Gulf. Moreover, the CRU dataset contains significantly wetter totals than GPCP in the Black Sea, Turkey, and Georgia region, yet it is significantly drier in the southern areas of Iraq and northern Saudi Arabia (compare Figure 2-1a & 2-1b). A lack of a dense observational network may result in the CRU dataset failing to capture accurately

the spatial distribution of rainfall in this southern region [Evans *et al.*, 2004]. Finally, it is important to note that although the CRU and GPCP results displayed in Figure 2-1 cover different time periods, looking at overlapping periods in both datasets reveal similar spatial distributions and magnitudes for annual precipitation.

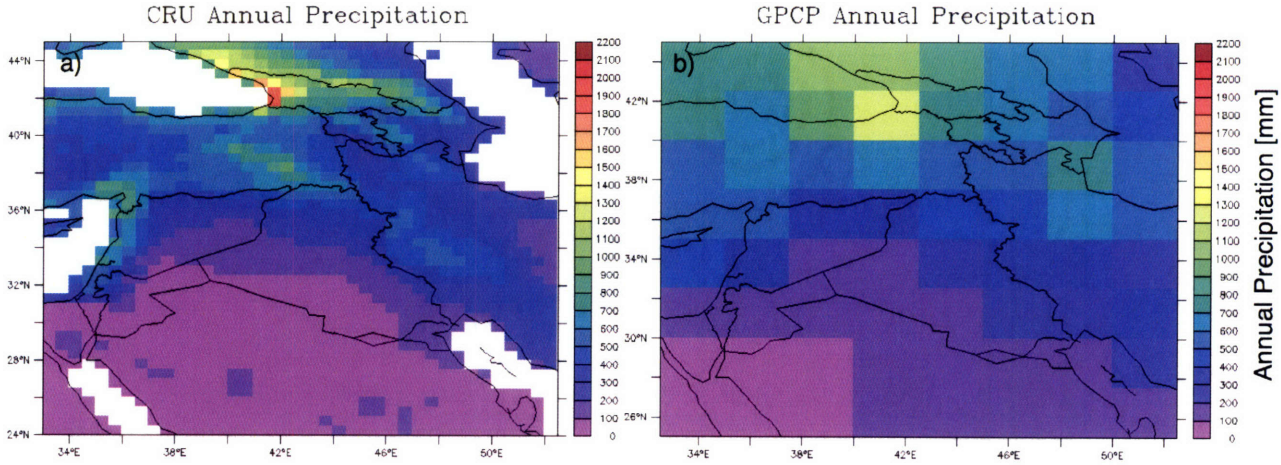

Figure 2-1: Average annual precipitation (mm) for the Middle East in a) CRU dataset ranging from 1952-2002 and b) GPCP dataset ranging from 1979-2004.

Yearly rainfall totals for Kuwait vary between the three datasets (see Table 2.2). Since Kuwait's rainy season occurs in the winter and spring months, annual rainfall values presented are determined from totaling June to May values. For example, annual rainfall for 1987 is calculated by summing rainfall from June of 1987 through May of 1988. While CRU and WMO annual totals of 112 and 114 mm are similar, GPCP's value of 188 mm is nearly 67% more than the other two datasets. GPCP's larger totals are also visible in the time series shown in Figure 2-3. In all but one year (1999), GPCP yearly values are larger than CRU. In fact, in above average rainfall years (i.e. 1992, 1994, 1995, and 1997), GPCP values are nearly double those of CRU (see Figure 2-3a). This trend is also visible at Kuwait City. In Figure 2-3b, a comparison is made between station data at Kuwait City airport (WMO) and the closest gridbox in the GPCP and CRU datasets that corresponds to the Kuwait City airport. Note how WMO estimates fall in between GPCP and CRU values in above average rainfall years. For example, in 1992, GPCP measures 353 mm for Kuwait while CRU measures only 155 mm. However, WMO falls in between these two estimates

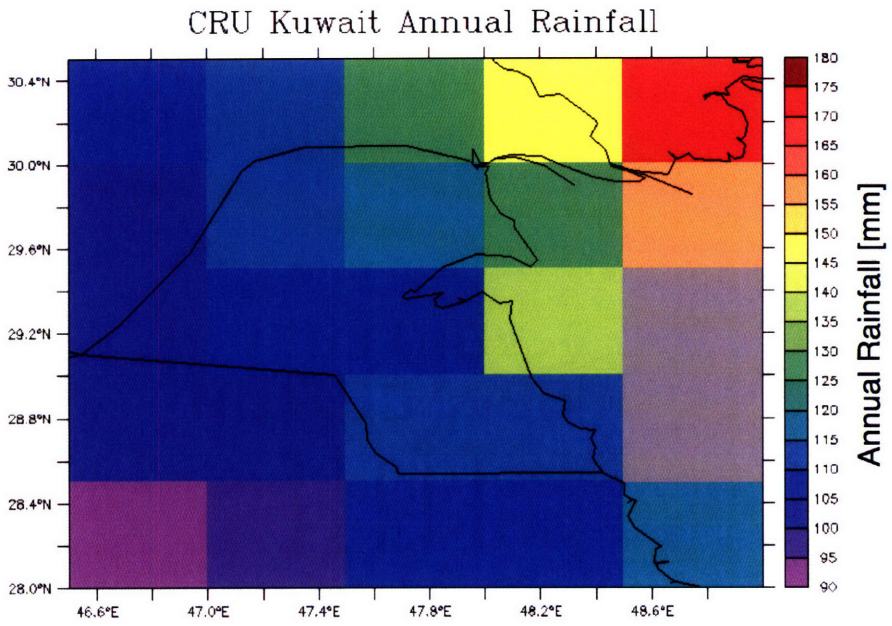

Figure 2-2: Average annual rainfall (mm) for Kuwait based on CRU 1952-2002 dataset. Note gray shaded gridboxes denote ocean/water data not included in the CRU dataset.

at 234 mm. In years before the advent of GPCP, the smoothing that occurs with CRU data is still noticeable. That is, WMO values for dry (below average rainfall) and wet (above average rainfall) years are more extreme than those of CRU. For instance, in the dry year of 1976, WMO recorded 43 mm of rainfall while CRU had nearly double this total at 73 mm. In contrast, the wet year of 1975 sees WMO rainfall of 260 mm while CRU's value is merely 190 mm (Figure 2-3b).

	CRU	GPCP	WMO
Temporal Coverage	1952-2002	1979-2004	1961-2002
Annual Rainfall μ [mm]	112	188	114
Standard Deviation σ [mm]	39	72	67
Coefficient of Variation C_v	0.35	0.38	0.59

Table 2.2: Summary of Kuwait rainfall for CRU, GPCP, WMO datasets.

2.2.2 Seasonal Cycle and Variability

Rainfall in Kuwait occurs in a relatively short, distinct, cool period during the winter months when synoptic scale systems originating from further north reach the region. This

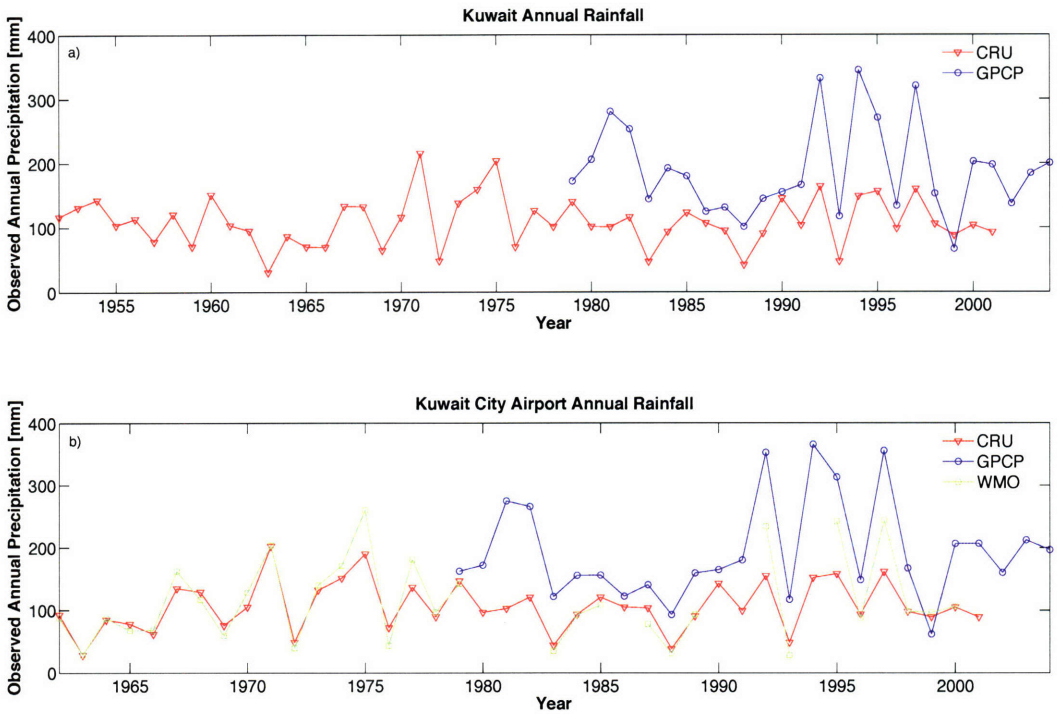

Figure 2-3: Time series of annual rainfall (mm) from CRU, GPCP, and WMO datasets for a) country of Kuwait and b) Kuwait City International Airport. Note that gridboxes in CRU and GPCP containing the airport's location are used in plot b).

period is detailed using CRU, GPCP, and WMO data (Figure 2-4). The seasonal cycle of rainfall in all three datasets is remarkably similar. Some of this similarity is most likely due to the WMO rain gauge contributing to both CRU averaging and GPCP merged values. Nevertheless, onset of appreciable rainfall occurs in November and subsides by April. Although detectable rainfall usually begins in November and ends in April, Al Kulaib [1984] describes rare occasions in which rainfall occurs in October and May. This is evident in Figure 2-4 with low average rainfalls but high standard deviations in these two months. In general, GPCP values are about 10 mm larger than both CRU and WMO estimates in each month of the rainy season. It is believed that the coarse resolution of GPCP, which includes wetter areas to the east in the Persian Gulf, results in rainfall totals larger than CRU and WMO values.

Both CRU and GPCP datasets have a double peak in rainfall occurring in January and March, where 27 mm of rain falls in either month (averaged between the datasets). In addition, a local minimum in February rainfall (17 mm) is seen in all three datasets. This seasonal pattern is most likely due to shifts in predominant storm track positions over Kuwait (Figure 2-5). During February, a more southerly storm track (from the Red Sea & Saudi Arabia) becomes dominant over the region. Consequently, a reduction in the frequency of large scale systems reaching the area from the stronger, (wetter) northerly storm track (by Syria & Israel) occurs [Walters, 1988]. This pattern is noticeable in Figures 2-5a and 2-5b, which show the high spatial correlation between Kuwait rainfall and rainfall in Syria and the eastern Mediterranean during the month of January. However, this connection decreases in February for both CRU and GPCP datasets. During this time, a new pattern of high spatial correlation between rainfall in Kuwait and the surrounding southern regions (Figures 2-5c & 2-5d) becomes prominent. More specifically, statistically significant correlations (at the 99% confidence level) are found with r-values above 0.50 (Figure 2-5d) over the Red Sea and central Saudi Arabia, revealing a larger connection with rainfall in this southern area. Therefore, since this drier, less active pattern becomes dominant in February, a reduction in rainfall is observed in Kuwait. However, by March, Figures 2-5e & 2-5f, correlation between Kuwait rainfall and precipitation to the north by Sryia and the eastern Mediterranean again increases; thus, Kuwait rainfall totals increase.

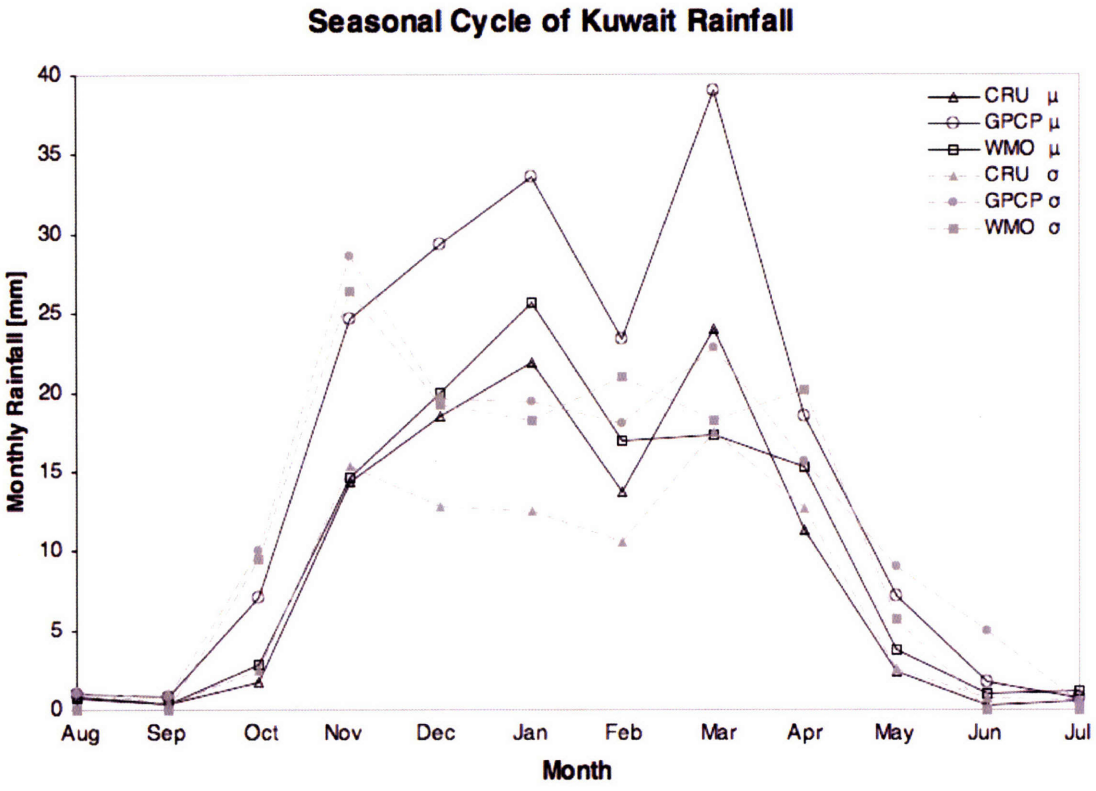

Figure 2-4: Seasonal cycle of rainfall in Kuwait for CRU and GPCP datasets and Kuwait City for WMO data. Monthly standard deviations are also plotted.

Lastly, Figure 2-4 highlights November, March, and April's large standard deviations for monthly rainfall. When averaged over the three datasets, these values translate into the largest coefficients of variation occurring in November and April (1.34 and 1.1, respectively). Since these months mark the transitional periods of the rainy season, which, in itself, varies from year to year, this relatively large spread about the mean is expected [Al Kulaib, 1984]. Furthermore, autocorrelation of Kuwait monthly rainfall at different lags is performed to determine if rainfall in one month is correlated with rainfall in a future month. However, results do not reveal any statistically significant persistence in monthly rainfall estimates over the country.

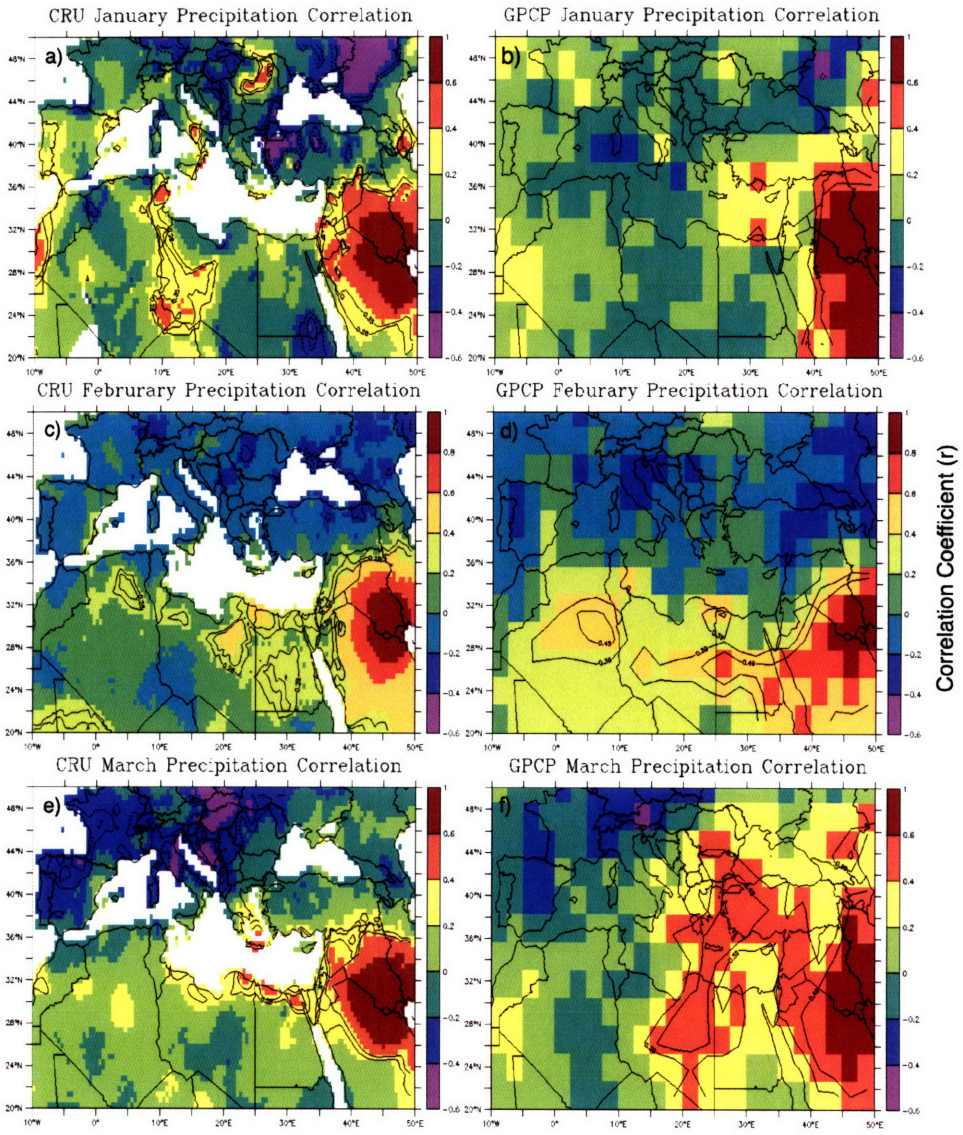

Figure 2-5: Spatial correlation between Kuwait rainfall and surrounding precipitation for a,c,e) CRU and b,d,f) GPCP for the months of January, February, and March respectively. Also contoured are the statistically significant correlation coefficients at the 95% and 99% confidence levels which correspond to r=+/-0.28 and r=+/-0.35, respectively, for CRU, and r=+/-0.38 and r=+/-0.49, respectively, for GPCP.

2.2.3 Interannual and Decadal Variability

The combined characteristics of the above datasets lead to a wide range in the estimates of interannual variability (refer to Table 2.2). As expected, CRU's standard deviation is lowest at 35 mm while GPCP,the highest at 72 mm, is more than double CRU's value. The airport data exhibits larger yearly variability than CRU but less than GPCP at 67 mm. Moreover, the coefficient of variation, C_v, is calculated to describe the dimensionless spread of values about the mean. Here, GPCP and CRU datasets have very similar values of C_v at 0.38 and 0.35, respectively. However, WMO data has a significantly larger value at nearly 0.60. A larger coefficient of variation at Kuwait City Airport seems logical since no averaging of rain gauges occurs as does in CRU and GPCP totals. In addition, as seen from CRU data in Figure 2-3, very little interdecadal variability occurs in Kuwait rainfall. However, the lack of a consistent, reliable dataset that extends throughout the twentieth century makes analyzing the decadal variability of rainfall in Kuwait challenging.

In addition, an analysis between annual and monthly Kuwait rainfall anomalies is performed. Results indicate that CRU's yearly Kuwait rainfall anomalies are highly correlated with March and April rainfall anomalies (see Figure 2-6). That is, nearly 36% of Kuwait annual rainfall variability can be explained by April rainfall anomalies (r=0.60) while 19% (r=0.44) can be explained by March anomalies. For example, in the CRU dataset, of the six wettest annual rainfalls, five of these years contain April rainfall values of at least 2.5 times the April average.

2.3 Discrepancies in Datasets

The discrepancy and wide range in values of the three observational datasets needs some explanation. In general, for above average years, WMO totals are larger than CRU. These larger values are due to localized convective events occurring at the airport which are muted in the CRU averaging [Al Kulaib, 1984]. In contrast, for years of below average rainfall, WMO reports values that are smaller than CRU. In these years, the majority of rainfall is most likely associated with northerly large scale depressions that travel across Kuwait and areas further north [Al Kulaib, 1984]. Therefore, CRU estimates, which have contributions

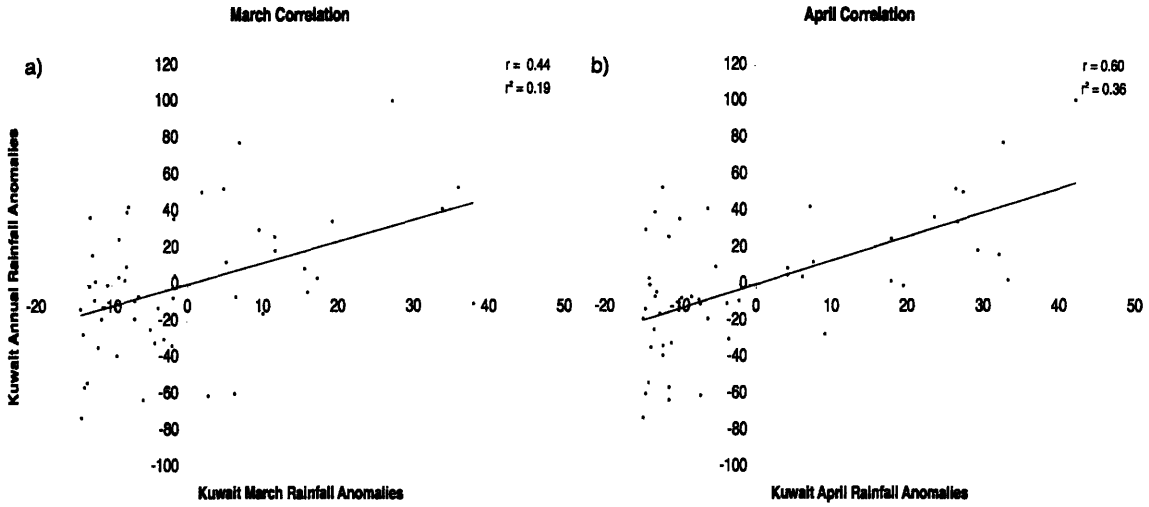

Figure 2-6: Monthly Kuwait rainfall anomalies for a) March and b) April plotted against yearly Kuwait rainfall anomalies for the past 50 years from CRU dataset. Also shown are the correlation coefficients (r) and the coefficients of determination (r^2), which are statistically significant at the 99% confidence level.

from stations north of Kuwait (where a denser network of observations exists), overestimate the actual Kuwait rainfall in such years. Hence, it will be of particular importance to include the WMO dataset when comparing model results to observations. Moreover, although both datasets have similar mean values, WMO contains a significantly larger standard deviation than CRU—74 mm versus 40 mm (Table 2.2). As a result, the coefficient of variation for WMO is nearly 65% larger than that of CRU, demonstrating the large smoothing that occurs in CRU averaging over multiple stations. In contrast, GPCP mean estimates are consistently larger than both CRU and WMO data. This difference is partly due to GPCP's coarser resolution and its use of satellite measurements for rainfall estimates. However, GPCP's C_v is similar to that of CRU yielding a similar spread about the mean. Explanations for these differences can be linked to the inherent characteristics and thus differences between the datasets. For example, with a gridbox of over 250 km in resolution, GPCP estimates rainfall over the Persian Gulf and coastal Iran whereas CRU & WMO are land based estimates at much finer resolutions (56 km and point estimate, respectively.) Therefore, GPCP's estimate for Kuwait represents a larger area that includes regions where annual rainfall is significantly larger than Kuwait (as can be discerned from plots of rainfall distribution in the region). However, as seen in Figure 2-3, when huge discrepancies do occur between CRU

and GPCP, airport rain gauge data consistently falls in between the two datasets. Therefore, the comparison to be made in this study using both CRU and WMO as benchmarks will be the best possible analysis for Kuwait rainfall.

2.4 Teleconnections with Tropical & Mid-Latitude Atmospheric Conditions

Much research has been done in studying the effects on regional climates of large scale atmospheric patterns such as the North Atlantic Oscillation-NAO [Hurrell, 1995] and the El Niño-Southern Oscillation-ENSO [Kumar *et al.*, 2006]. For example, Cullen *et al.* [2002] examine the effects of the NAO teleconnection on streamflows of the Middle East at the interannual and decadal timescale. However, in this study, no significant relationship between Kuwait rainfall and NAO is found at a monthly or yearly timescale. These results are similar to those of Evans *et al.* [2004] which does not find significant correlation between NAO and rainfall in the Middle East.

Nevertheless, studies have shown connections do exist between ENSO anomalies and precipitation in Israel [Price *et al.*, 1998]. In a similar analysis, the correlation between the Southern Oscillation Index (SOI) and normalized annual rainfall anomalies in Kuwait is performed using both CRU and GPCP datasets (see Figure 2.7). Results indicate that a statistically significant negative relationship between SOI and Kuwait rainfall exists in both datasets (r=-0.40 and r=-0.48, respectively). That is, in El Niño years (negative SOI indices), when Pacific Ocean sea surface temperature anomalies are positive, Kuwait's annual rainfall is above average. Nevertheless, the relationship is somewhat weak where only 16% of the variability in CRU annual rainfall can be explained by the ENSO phenomenon whereas 23% of rainfall variability in GPCP is explained (Figure 2.7). Interestingly, this relationship extends only for the past twenty-five years. Extending the analysis for longer periods of time causes a significant decrease in correlation between ENSO and Kuwait annual rainfall. A similar finding was reported by Price *et al.* [1998]. Many studies [e.g. Rajagopalan *et al.* [1997], and Wuethrich [1995]] have documented recent changes in fre-

quency of El Niño events and the increased connection between Pacific and mid-latitude ocean-atmosphere systems. These changes may help explain the limited nature of the correlations observed between ENSO and Kuwait rainfall [Price *et al.*, 1998]. Lastly, noting the strong relationship between April and March rainfall anomalies and annual rainfall, a connection between NAO (or SOI) and March/April rainfall is studied. However, no significant correlation is found between these large scale atmospheric features and these monthly rainfall values.

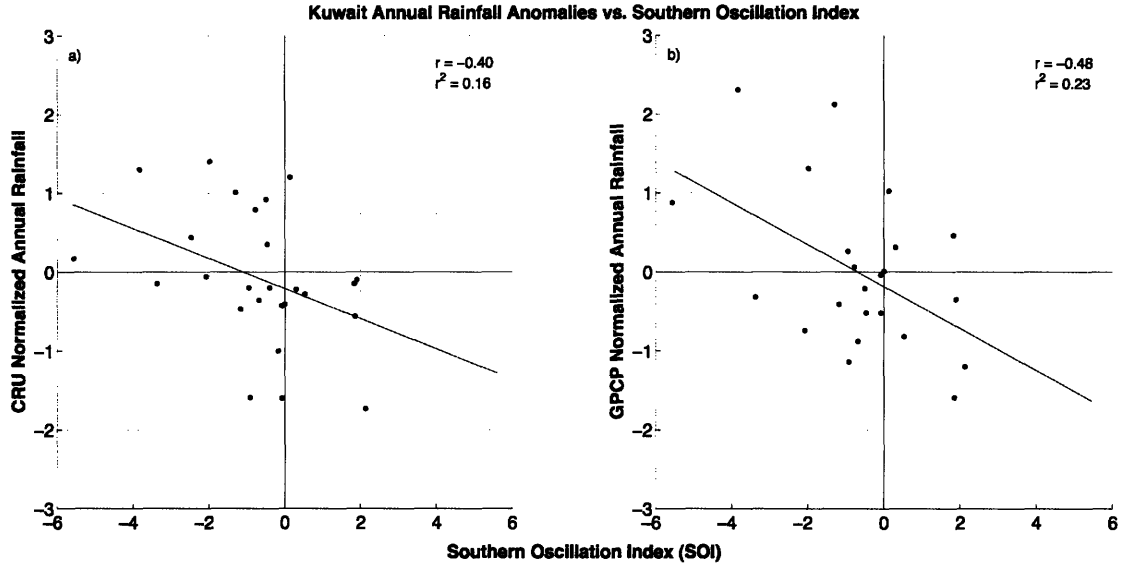

Figure 2-7: Scatter plots showing correlation between average Southern Oscillation Index for October through March and Kuwait normalized annual rainfall anomalies in a) CRU (1976-2001) and b) GPCP (1979-2001). Also plotted are the best fit lines, correlation coefficient (r), and coefficient of determination (r^2). Note that these correlations are significant at the 95% confidence level.

Moreover, interannual variability of Kuwait rainfall can be explained by rainfall variability in the mid-latitudes of Europe. More specifically, Figure 2-8 highlights the spatial correlation between Kuwait rainfall summed from November to April and the corresponding European rainfall in the CRU datatset. As seen, a statistically significant negative correlation occurs between rainfall in Eastern Europe/Eurasia and rainfall in Kuwait during this period. In fact, a negative correlation between rainfall in Eurasia and rainfall in Kuwait is also evident at the monthly timescale in both CRU & GPCP datasets (Figure 2-5). In contrast, a positive correlation between Kuwait rainfall and rainfall in northern Africa and

the eastern Mediterranean is observed in Figure 2-8. Likewise, this positive relationship is seen throughout the rainy season (see Figure 2-5). Most likely, cyclogenesis in the eastern Mediterranean causes the positive correlation in the region where resulting storm systems migrate toward Kuwait, causing much of the country's rainfall. It is important to mention that a similar analysis to that of Figure 2-8 with GPCP data used does not reveal as clear or as strong correlation pattern as that of the CRU dataset.

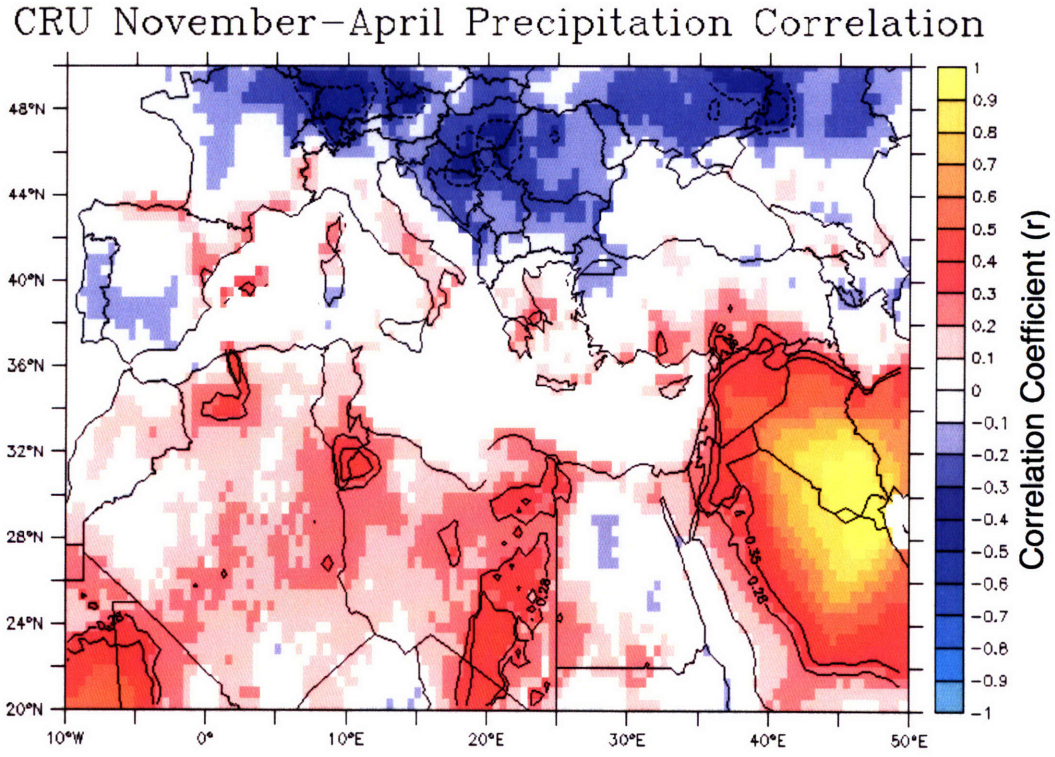

Figure 2-8: Spatial correlation between CRU's Kuwait rainfall and surrounding precipitation for November through April period. Note contours for statistically significant correlation coefficients at the 95% and 99% confidence levels which correspond to r=+/-0.28 and r=+/-0.35, respectively.

Chapter 3

Regional Climate Model version 3 (RegCM3)

The following chapter provides a broad overview of the history and features of the regional climate model (RCM) used in this study, Regional Climate Model 3 (RegCM3). In this study, RegCM3 is used to simulate the climate of Kuwait.

3.1 Model Description

In an ideal numerical and computational environment, climate model simulations would extend globally as well as compute atmospheric and surface physics at the finest horizontal, vertical, and temporal resolutions. However, in reality, such a scenario is computationally infeasible. Therefore, RCMs attempt to find accord between temporal resolution and domain size while maintaining realistic computational times. In order to maintain numerical stability, temporal resolution, Δt, becomes a function of both grid cell size (the aforementioned horizontal and vertical resolutions—Δx), and maximum wind velocity, u. This relationship, also known as the Courant-Freidrichs-Levy condition for stability, is better described numerically as:

$$\frac{u\Delta t}{\Delta x} \leq 1 \tag{3.1}$$

A limited area regional climate model (LAM) is driven by time-dependent lateral boundary conditions and initial conditions derived from a general circulation model (GCM) simulation or reanalysis product [Elguindi *et al.*, 2004]. Such high resolution models utilize one-way nesting, where the LAM has no feedback on the coarse meteorological forcings at the boundaries. Rather, these forcings simply provide initial and boundary conditions for the regional model. As a result, regional climate models, like RegCM3, are able to perform at resolutions on the order of kilometers (10 km for RegCM3, where some numerical weather prediction models can reach even finer resolutions than this), while GCMs have spatial resolutions on the order of hundreds of kilometers (approximately 1°). The ability to simulate climates at high spatial resolution offers significant advantages for studying regional weather patterns [Giorgi *et al.*, 1998]. For example, with finer spatial resolutions, topography as well as mesoscale meteorological features are better represented, both which can markedly affect local climates. However, one must realize that while RegCM3 represents an important tool for examining environmental sensitivity to climate variability [e.g. changes in precipitation, atmospheric radiation], independently, RegCM3 cannot be used to predict climate change. Rather, RegCM3 must be forced by climate change scenarios from GCM simulations to achieve such a sensitivity analysis.

Originally developed at the National Center for Atmospheric Research (NCAR), but now maintained at the International Center for Theoretical Physics (ICTP), RegCM3 is a three-dimensional, hydrostatic, compressible, primitive equation, sigma-coordinate (Figure 3-1), RCM. RegCM3 traces its ancestry from NCAR's RegCM, which was developed from the work of Dickinson *et al.* [1989], Giorgi and Bates [1989], and Giorgi [1990]. The model maintains much of the dynamical core of NCAR/Pennsylvania State University's (PSU/NCAR) mesoscale model, MM4 [Anthes *et al.*, 1987].

From developments made to RegCM3 itself, to its coupling with hydrologic, aerosol, and dynamic vegetation models, RegCM3 has become a powerful tool for regional climate

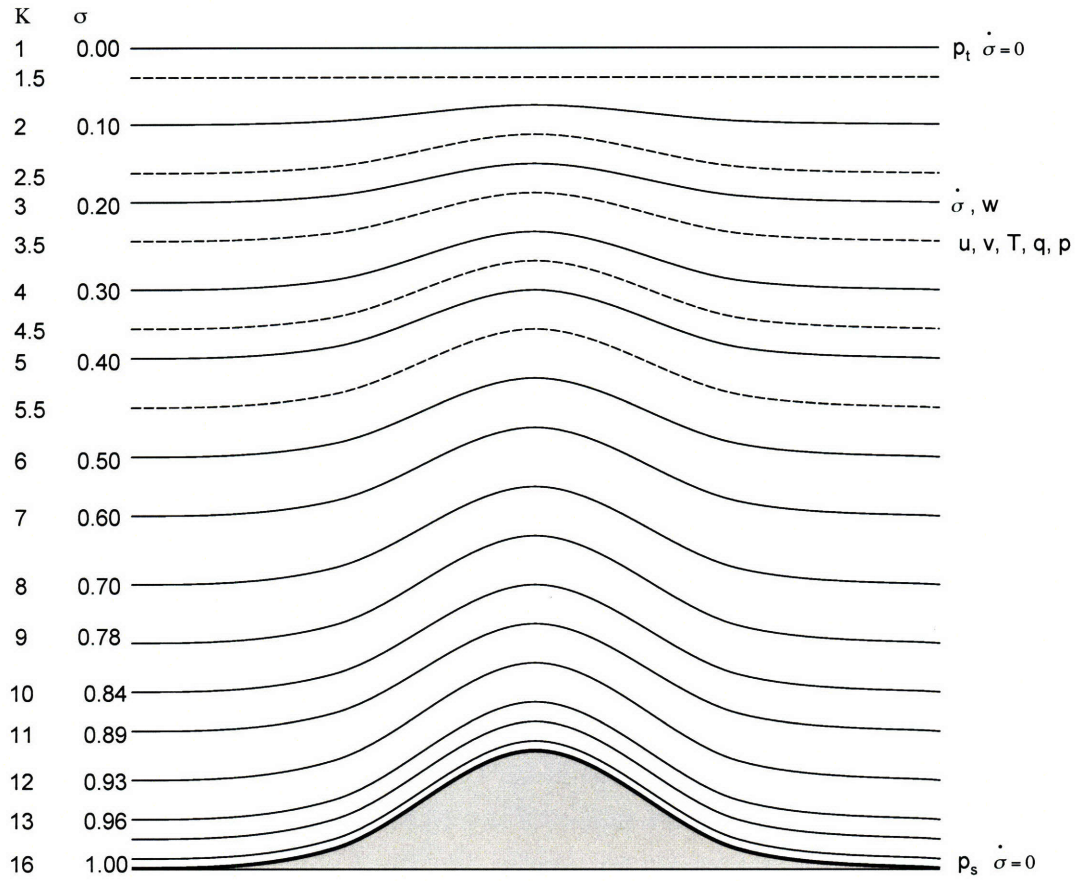

Figure 3-1: Diagram showing terrain-following vertical structure of RegCM3. Example given for a 16 vertical layer sigma-coordinate model (RegCM3 offers 18 levels). Dashed lines denote half-sigma levels, solid lines denote full-sigma levels [Winter, 2006]. (Adapted from the PSU/NCAR Mesoscale Modeling System Tutorial Class Notes and User's Guide).

studies [Winter, 2006]. RegCM originally contained the radiation package of NCAR's Community Climate Model version 1 (CCM1) of Dickinson *et al.* [1986]; Giorgi [1990] , a medium resolution local planetary boundary layer (PBL) scheme, the cumulus convection scheme (Kuo scheme) of Anthes [1977], Biosphere-Atmosphere Transfer Scheme (BATS) [Dickinson *et al.*, 1986], and the explicit moisture large-scale precipitation scheme of Hsie *et al.* [1984].

In 1993, RegCM was further updated to Regional Climate Model version 2 (RegCM2) which contained many significant improvements adapted from both PSU/NCAR's Mesoscale Model version 5 (MM5) [Grell *et al.*, 1994] and NCAR's Community Climate Model version 2 (CCM2) [Hack *et al.*, 1993]. The original radiation scheme was updated using the radiation physics of CCM2 which employs a δ-Eddington approach and includes the effects of H_2O, O_3, O_2, CO_2, and clouds on short and longwave radiation [Briegleb, 1992]. A new mass flux convection scheme, developed by Grell [1993], was added, as well as the local PBL scheme replaced by a non-local PBL parameterization of Holtslag *et al.* [1990]. Lastly, surface physics were improved in RegCM2 with the inclusion of BATS1e [Dickinson *et al.*, 1993], the latest version of BATS.

From RegCM2, multiple improvements were made to create the current version of the model, RegCM3. Again, the atmospheric radiation transfer package was updated to NCAR's Community Climate Model version 3, CCM3, based on the work of Kiehl *et al.* [1996]. The CCM3 radiation package incorporates the effects of additional greenhouse gases (NO_2, CH_4, CFCs), atmospheric aerosols, and cloud ice [Elguindi *et al.*, 2004]. A reduced version of Hsie *et al.*'s fully explicit moisture scheme, the Simplified Explicit Moisture Scheme (SIMEX), was also included in RegCM3 to decrease the computational expense caused by calculations for large scale precipitation [Giorgi and Shields, 1999]. SIMEX differs from Hsie *et al.*'s scheme by eliminating the prognostic variable for rainwater and its associated calculation while still maintaining the cloud water variable used directly in the cloud radiation physics. In addition, Giorgi and Shields's SIMEX adds fundamental interactions between the hydrologic cycle and the energy budget [Elguindi *et al.*, 2004]. RegCM2's dynamical core, planetary boundary layer scheme (Holtslag *et al.*), and land surface physics (BATS1e) were left unchanged in RegCM3 [Elguindi *et al.*, 2004]. In

addition to the aforementioned changes in some of RegCM's model physics, several new features were added to the model. More specifically, a new ocean flux parameterization by Zeng *et al.* [1998] was added, the lake model of Small and Sloan [1999] was coupled to RegCM3, and an aerosol/dust chemical tracer model was introduced. Moreover, the Subgrid Explicit Moisture Scheme (SUBEX), a non-convective, resolvable-scale cloud and precipitation scheme was included and subsequently replaced SIMEX [Pal *et al.*, 2000]. Additionally, a new convection package, MIT's Emanuel scheme [1991], was added to RegCM3. With the Emanuel scheme, RegCM3 now offers a total of three possible representations of non-resolvable cumulus convection, including the Grell scheme from RegCM2 and the Kuo scheme from RegCM. More information regarding the specific parameterization schemes, history, and applications of RegCM3 can be found in the RegCM3's User Guide of Elguindi *et al.* [2004].

3.2 Model Dynamics

RegCM3 works on the basic governing equations of atmospheric motions. Essentially, RegCM3 implements conservation of mass, energy, momentum, and water vapor while assuming air behaves as an ideal gas. The model's dynamic equations and numerical discretizations are best described by Grell *et al.* [1994]. Below are the relative equations that describe the atmospheric dynamics in RegCM3:

Horizontal Momentum Equations

$$\frac{\partial p^* u}{\partial t} = -m^2 \left(\frac{\partial p^* uu/m}{\partial x} + \frac{\partial p^* vu/m}{\partial y} \right) - \frac{\partial p^* u\dot{\sigma}}{\partial \sigma} - mp^* \left[\frac{RT_v}{(p^* + p_t/\sigma)} \frac{\partial p^*}{\partial x} + \frac{\partial \phi}{\partial x} \right] + fp^* v + F_H u + F_V u \tag{3.2}$$

and,

$$\frac{\partial p^* v}{\partial t} = -m^2 \left(\frac{\partial p^* uv/m}{\partial x} + \frac{\partial p^* vv/m}{\partial y} \right) - \frac{\partial p^* v\dot{\sigma}}{\partial \sigma} - mp^* \left[\frac{RT_v}{(p^* + p_t/\sigma)} \frac{\partial p^*}{\partial y} + \frac{\partial \phi}{\partial y} \right] + fp^* u + F_H v + F_V v \tag{3.3}$$

where, the east-west and north-south components of velocity are u and v, respectively, T_v is the virtual temperature, ϕ is the geopotential height, f is the coriolis parameter, R is the gas constant for dry air, m is the map scale factor for Lambert Conformal, Stereographic, or Mercator map projections, $\dot{\sigma} = \frac{d\sigma}{dt}$, F_H and F_V represent the horizontal and vertical diffusion, respectively and lastly, $p^* = p_s - p_t$, where p_s is the surface pressure and p_t is the top of atmosphere pressure, which is specified as 5 mb in RegCM3.

Continuity Equation

Vertical integration of Equation 3.4 yields the temporal variation of the surface pressure in RegCM3. Therefore, after calculating the surface pressure tendency, $\frac{\partial p^*}{\partial t}$, the vertical velocity in sigma coordinates, $\dot{\sigma}$, can be computed at each level in the model as such 3.4 [Elguindi *et al.*, 2004]:

$$\frac{\partial p^*}{\partial t} = -m^2 \left(\frac{\partial p^* u/m}{\partial x} + \frac{\partial p^* v/m}{\partial y} \right) - \frac{\partial p^* \dot{\sigma}}{\partial \sigma} \tag{3.4}$$

$$\dot{\sigma} = -\frac{1}{p^*} \int_0^\sigma \left[\frac{\partial p^*}{\partial t} + m^2 \left(\frac{\partial p^* u/m}{\partial x} + \frac{\partial p^* v/m}{\partial y} \right) \right] d\sigma' \tag{3.5}$$

where σ' is a dummy variable of integration and $\dot{\sigma}(\sigma = 0) = 0$ [Elguindi *et al.*, 2004]

Thermodynamic and Omega (ω) Equation

The thermodynamic equation can be written as follows:

$$\frac{\partial p^* T}{\partial t} = -m^2 \left(\frac{\partial p^* u T/m}{\partial x} + \frac{\partial p^* v T/m}{\partial y} \right) - \frac{\partial p^* T \dot{\sigma}}{\partial \sigma} + \frac{R T_v \omega}{C_{pm}(\sigma + P_t/p_{ast})} + \frac{p^* Q}{C_{pm}} + F_H T + F_V T \tag{3.6}$$

where, C_{pm} is the specific heat for moist air (at constant pressure) and is defined as $C_{pm} = C_p(1 + 0.8q_v)$, Q is the diabatic heating term, $F_H T$ represents horizontal diffusion while $F_V T$ represents the effect of vertical mixing and the dry convective adjustment [Elguindi *et al.*, 2004]

ω is defined as:

$$\omega = p^* \dot{\sigma} + \sigma \frac{dp^*}{dt} \tag{3.7}$$

and, by definition, the total derivative for p^*:

$$\frac{dp^*}{dt} = \frac{\partial p^*}{\partial t} + m \left(u \frac{\partial p^*}{\partial x} + v \frac{\partial p^*}{\partial y} \right) \tag{3.8}$$

Hydrostatic Equation

Geopotential heights are calculated from the hydrostatic equation using the virtual temperature, $T_v = T(1 + 0.608\ q_v)$ where, q_v, q_c, and q_r are the water vapor, cloud water/ice, and rain water/snow mixing ratios.

$$\frac{\partial \phi}{\partial \ln(\sigma + p_t/p^*)} = -RT_v \left[1 + \frac{q_c + q_r}{1 + q_v} \right] \tag{3.9}$$

3.3 Radiation Scheme

As mentioned prior, RegCM3 employs the radiation scheme of NCAR's CCM3. The radiation package is called at intervals of 30 minutes regardless of the temporal or spatial resolution of the simulation [Elguindi *et al.*, 2004]. Fluxes for longwave, shortwave, and surface radiative energy components are held constant between intervals [Kiehl *et al.*, 1996]. With a top down approach, insolation at the top of atmosphere (TOA), S_I, can be expressed as:

$$S_I = S_0 \epsilon \cos\zeta \tag{3.10}$$

where S_0 is the solar constant, ϵ is the eccentricity factor, and ζ is the solar zenith angle [Kiehl *et al.*, 1996]. Within RegCM3, the diurnal cycle is calculated as exactly 24 hours long, while the calendar year contains exactly 365 days. These are calculated by the following equations:

$$\cos\zeta = \sin\phi\sin\delta - \cos\phi\cos\delta\cos(2\pi t_{local}) \tag{3.11}$$

$$\begin{aligned}\cos\epsilon =& 1.000110 + 0.034221\cos\theta_0 + 0.001280\sin\theta_0 + 0.000719\cos 2\theta_0 \\ &+ 0.000077\sin 2\theta_0\end{aligned} \tag{3.12}$$

$$\begin{aligned}\delta =& 0.006918 - 0.399912\cos\theta_0 + 0.070257\sin\theta_0 - 0.006758\cos 2\theta_0 \\ &+ 0.000907\sin 2\theta_0 - 0.002697\cos 3\theta_0 + 0.001480\sin 3\theta_0\end{aligned} \tag{3.13}$$

where θ_0 represents the mean orbit angle, ϕ is the latitude in radians, δ symbolizes the solar declination in radians, and t_{local} is the calendar day in local time [Kiehl *et al.*, 1996]. The

formulation of $\cos\zeta$ is taken from Sellers [1965] and equations for ϵ and δ are drawn from Paltridge and Platt [1976].

Once TOA solar insolation is calculated, RegCM3's radiation scheme determines the fraction of TOA energy that reaches the surface. From this value and surface characteristics, RegCM3 determines the portion of that energy which is reflected by the surface, the albedo. This calculation is performed using the δ-Eddington approximation, originally attributed to both Joseph *et al.* [1976] and Coakley Jr. *et al.* [1983], but fully documented in Briegleb [1992].

The scheme divides the solar spectrum into 18 spectral intervals, each spectral interval covers wavelengths important for radiatively relevant interactions with atmospheric chemistry (7 for O_3, 1 for visible, 7 for H_2O, 3 for CO_2) [Kiehl *et al.*, 1996]. Each layer of the atmosphere in RegCM3 (Figure 3-1) is modeled as a well-mixed (homogeneous) blend of all radiatively significant elements. From here, reflectivity and transmissivity are calculated for each layer, and then combined together allowing scattering between layers [Kiehl *et al.*, 1996]. This calculation produces the spectral fluxes (upward and downward) at each layer interface, which then accumulate over multiple spectral intervals which yields broad band fluxes. Subsequently, these broad band fluxes are used to determine the radiative heating rate and the cosine of the solar zenith angle, both key inputs to other schemes [e.g. Dickinson's BATS1e, Zeng's ocean flux parameterization] found in RegCM3.

Based on Ramanathan and Downey's [1986] absorptivity and emissivity formulation, fluxes of longwave radiation ($F^{\downarrow}\&F^{\uparrow}$) are calculated as follows:

$$F^{\downarrow}(p) = B(0)\varepsilon(0,p) + \int_0^p \alpha(p,p')dB(p') \tag{3.14}$$

and,

$$F^{\uparrow}(p) = B(T_s) - \int_p^{p_s} \alpha(p,p')dB(p') \tag{3.15}$$

where B is the Stefan-Boltzmann relation

$$B(T) = \sigma T^4 \tag{3.16}$$

T is temperature, T_s is surface temperature, σ is the Stefan-Boltzmann constant, α is the absorptivity, ε is the emissivity, p_s is surface pressure, and p, p' are pressures [Kiehl *et al.*, 1996].

While the δ-Eddington approximation calculates absorption of radiative energy for multiple atmospheric gases [i.e. CO_2, O_3, etc.], the effect of clouds on solar radiation is parameterized by the work of Slingo [1989] and Ebert and Curry [1992]. More specifically, for cloud droplets that are in the form of liquid water, optical properties of clouds [e.g. single scattering albedo, asymmetry parameter, extinction optical depth, forward scattering parameter] are calculated based on the cloud water path and droplet effective radius. The cloud water path (CWP) is inputed into the radiation package from both the convective and large-scale precipitation schemes [Kiehl *et al.*, 1996]. It is important to note that the cloud radiative properties depend on the phase of water [i.e. liquid water (warm) cloud or ice (cold) cloud] and calculated at each individual spectral interval [Kiehl *et al.*, 1996]. However, when partial cloudiness occurs or clouds overlap, a simplified parameterization which complies with the random overlap assumption, benchmarked by Briegleb [1992], is implemented by RegCM3.

For a full description of the radiation package within RegCM3, please refer to Kiehl *et al.* [1996].

3.4 Boundary Layer Physics

Holtslag's [1990] non-local planetary boundary layer (PBL) scheme, contained in NCAR's CCM3, is also used to parameterize boundary layer physics in RegCM3. As mentioned above, before using Holtslag *et al.*'s work, a local diffusion scheme was included in RegCM [Elguindi *et al.*, 2004]. The local diffusion scheme assumes that the flux of any substance [e.g. momentum, water vapor, latent heat] caused by turbulence can be determined by

the local gradient of that given quantity [Kiehl *et al.*, 1996]. This assumption holds true when the height of the PBL is larger than the length scale of the largest turbulent eddies. However, the assumption breaks down for relatively large turbulent eddies where the flux can actually run opposite to the local gradient [Kiehl *et al.*, 1996; Deardorff, 1972; Holtslag and Moeng, 1991]. Large eddies, which are often associated with unstable or convective atmospheric conditions, are, in general, poorly represented by local diffusion schemes as that used prior to RegCM3. Therefore, it becomes necessary to employ a non-local PBL parameterization [Kiehl *et al.*, 1996]. In a non-local PBL scheme, the diffusion is modified in such a way that the vertical eddy flux of a substance C [e.g. momentum, water vapor, latent heat], $\overline{w'C'}$, at a given height z is described by:

$$\overline{w'C'} = -K_c \left(\frac{\partial C}{\partial z} - \gamma_c \right) \tag{3.17}$$

and, K_c is calculated from:

$$K_c = k w_t z \left(1 - \frac{z}{h} \right)^2 \tag{3.18}$$

where, w_t is the turbulent velocity scale ($\approx$ 40 m in RegCM3), k is the von Karman constant, and h is the PBL height solved iteratively using:

$$h = \frac{Ri_{cr}[u(h)^2 + v(h)^2]}{(g/\theta_s)(\theta_v(h) - \theta_s)} \tag{3.19}$$

in Equation 3.19, the critical bulk Richardson number for the PBL is represented by Ri_{cr}, $u(h)$ and $v(h)$ are the horizontal velocity components at height, h, g is the acceleration due to gravity, $\theta_v(h)$ is the virtual temperature at h, and θ_s is a measure of the surface air temperature, calculated from:

For unstable conditions (i.e., Monin-Obukhov height, L, is less than 0) [Holtslag *et al.*,

1990]:

$$\theta_s = \theta_v(z_s) + K\frac{\overline{w'\theta'_o}}{w_t} \tag{3.20}$$

and, for stable conditions:

$$\theta_s = \theta_v(z_s) \tag{3.21}$$

where z_s is located at 2m, K is a constant equal to 8.5, and $\overline{w'\theta'_o}$ is the surface heat flux. The term $K\frac{\overline{w'\theta'_o}}{w_t}$ represents the convective thermals strength located at the lower part of the PBL, and hence is zero for stable conditions [Holtslag *et al.*, 1990].

Lastly, γ_c, the countergradient transport, represents the non-local transport of both heat and moisture ($C = \theta$,q, respectively) from dry convection:

$$\gamma_c = K\frac{\overline{w'C'_o}}{w_t h} \tag{3.22}$$

where $\overline{w'C'_o}$ is the surface temperature or water vapor flux. This equation is used from the top of the surface layer ($0.1h$) to the top of the PBL in RegCM3 [Elguindi *et al.*, 2004]. For heights higher than the top of the PBL or for stable conditions, γ_c is neglected [Elguindi *et al.*, 2004].

3.5 Convection Schemes

Since atmospheric convection occurs at horizontal resolutions on the order of 1 kilometer or less, most models are required to parameterize this process by assuming that the statistical properties of convection can be deduced from large resolvable scale processes. RegCM3 offers a total of three such convection schemes: the Kuo scheme [Anthes, 1977]; the Grell scheme [Grell, 1993]; and the Emmanuel scheme [Emanuel, 1991]. The Grell

scheme offers two different closure assumptions: the Arakawa & Schubert closure (AS74) [Grell *et al.*, 1994] or the Fritsch & Chappell closure (FC80) [Fritsch and Chappell, 1980]. Although results presented in this study implement both the Grell scheme with the FC80 closure and the Emanuel scheme, the Kuo scheme is mainly used in simulations of precipitation over the Middle East due to its superior performance over the domain. Nevertheless, a detailed description of all three schemes will be included. Full documentation and references for all convection schemes can be found in Elguindi *et al.* [2004].

3.5.1 Kuo Scheme

Developed by Anthes [1977], and later simplified by Anthes *et al.* [1987] to be included in PSU/NCAR's MM4, the Kuo scheme, named for the work of Kuo [1974], is triggered when the total horizontal moisture convergence exceeds a critical threshold value [Anthes, 1977]. Figure 3-2 depicts a simple diagram of the fundamental processes that occur in the Kuo scheme.

The vertically integrated moisture convergence, M_t, is calculated as:

$$M_t = \left(\frac{m^2}{g}\right) \int_0^1 \frac{\nabla p^* \dot{V} q_v}{m} d\sigma \tag{3.23}$$

where m is the mass flux, g is acceleration due to gravity, ∇p^* is a function of surface and top of model pressure, $\dot{V}$ is dependent on horizontal velocity, q_v is the mixing ratio of water vapor, and σ is the vertical sigma level.

The vertically integrated moisture convergence term, M_t, only includes the advective tendencies for water vapor. However, a potential feedback between rainfall in a prior time step and current moisture convergence can occur. That is, evapotranspiration from a prior time step is indirectly included in the moisture convergence since it will moisten the lower atmosphere. As a result, as evapotranspiration increases, more and more of it can be recycled into rainfall, assuming that the column remains convectively unstable [Pal, 2001].

As shown in Figure 3-2, a fraction of the total moisture convergence in the cumulus convection is converted to precipitation, R:

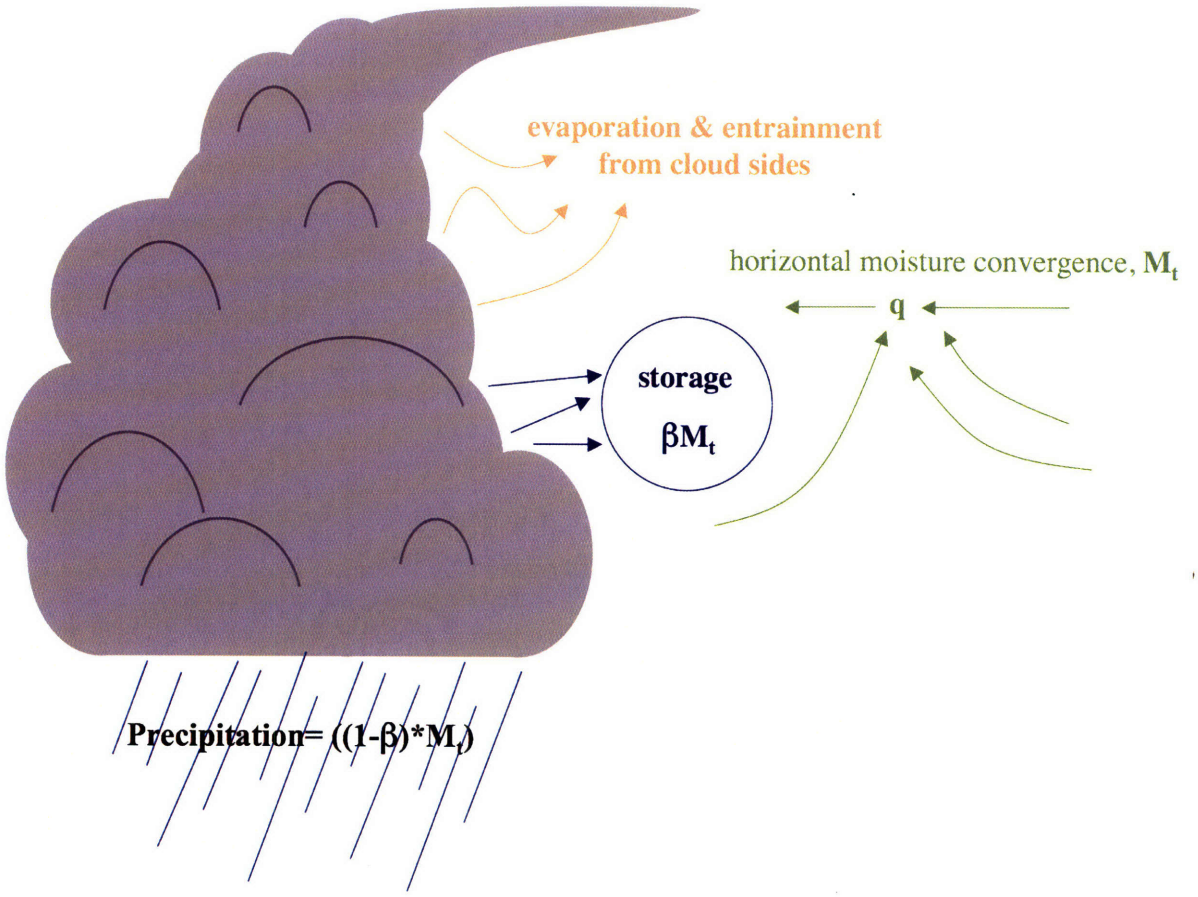

Figure 3-2: Diagram of the Kuo scheme [Anthes, 1977].

$$R = M_t(1 - \beta) \tag{3.24}$$

where β is the precipitation efficiency factor which is a function of the average relative humidity $\overline{RH}$ as follows:

$$\begin{aligned} \beta &= 2(1 - \overline{RH}) && \overline{RH} \geq 0.5 \\ &= 1 && \text{otherwise} \end{aligned} \tag{3.25}$$

The remaining fraction, β, remains in and thereby moistens the column [Anthes, 1977]. In theory, the transfer of latent heat from condensed water (that is subsequently reevaporated before escaping from the cloud) should be distributed as a function of both the height of condensation and reevaporation [Anthes, 1977]. However, this process is parameterized in the Kuo scheme by dividing the latent heat from condensation along the cloud using a parabolic heating profile, which allocates the maximum heating to the upper part of the cloud [Pal, 1997].

Lastly, some computational modifications to the Kuo scheme were made by both Giorgi and Bates [1989] and Giorgi and Marinucci [1991] to eliminate numerical point storms by including a horizontal diffusion term and a time release constant (so that moisture and latent heat are not redistributed instantaneously).

3.5.2 Grell Scheme

Similar in structure to the Arakawa & Schubert convective scheme [1974], the Grell scheme offers a basic representation of cumulus convection. Triggered when a lifted parcel of air attains moist convection, the Grell scheme has been most successfully and widely used over domains of the Midwest United States of America. As shown in Figure 3-3, the scheme simply models clouds as two steady-state circulations: an updraft and a downdraft [Grell *et al.*, 1994].

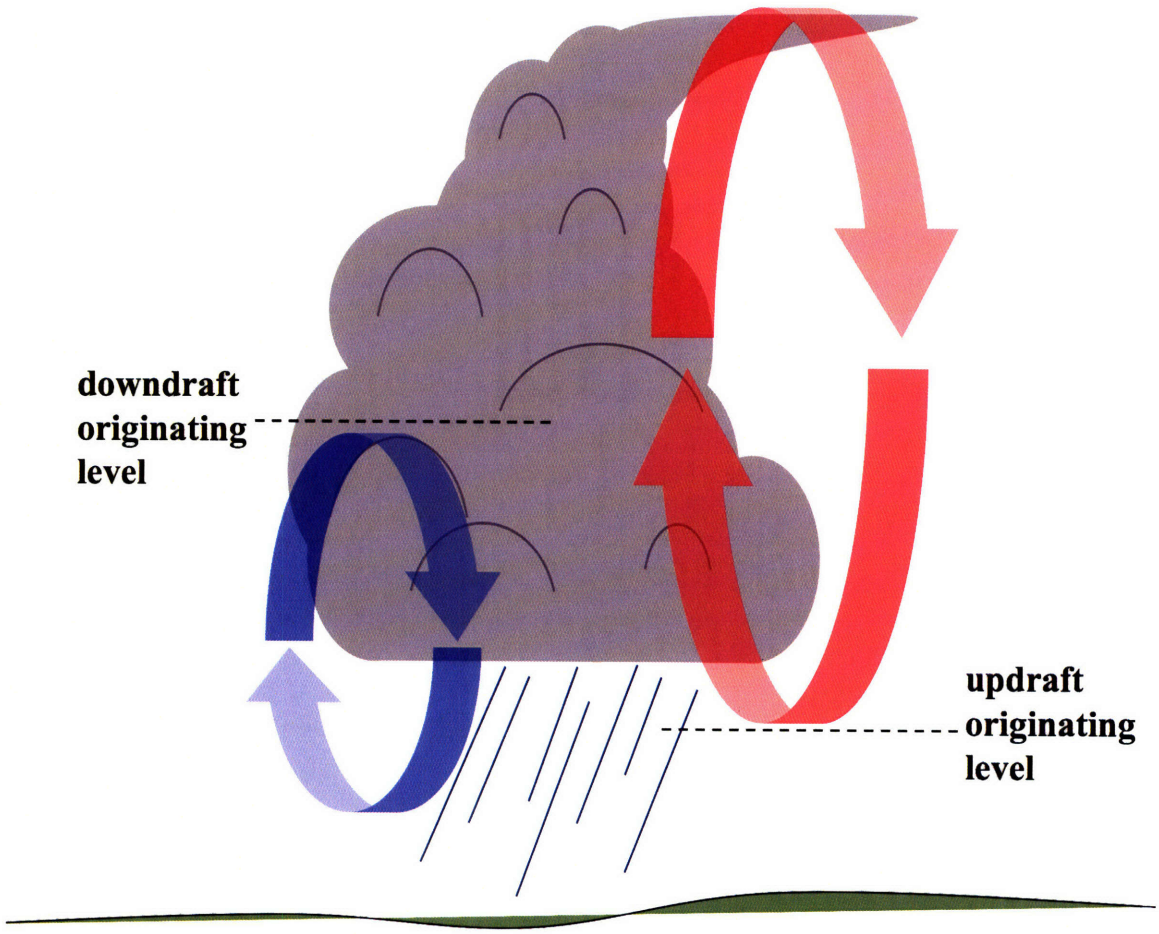

Figure 3-3: Conceptual diagram of the Grell scheme adapted from Grell *et al.* [1994].

It is important to note that no mixing is allowed between the cloudy air and the environmental air along the length of the column, rather it is allowed only at the top and bottom of the circulations [Grell *et al.*, 1994]. Therefore, entrainment or detrainment from the sides of a cloud is prohibited. In arid regions, this may be an important process that is ignored in the Grell scheme. In addition, mass flux, $m_{u,d}$ is held constant with height, z ,and since no entrainment or detrainment occurs along the edges of the cloud, this can be represented numerically as:

for the updraft:

$$m_u(z) = m_u(z_b) = m_b \tag{3.26}$$

and, for the downdraft:

$$m_d(z) = m_d(z_0) = m_0 \tag{3.27}$$

where m_u and m_d represent the updraft and downdraft mass flux, respectively, z_b the originating level of the updraft mass flux, and z_0 is the originating level of the downdraft mass flux. Also, m_b and m_0 are the mass fluxes of the updraft and downdraft at their originating levels [Grell *et al.*, 1994]. Maximum and minimum moist static energy values dictate the originating levels, h, for both the updraft and downdraft. Mathematically, this is expressed as:

$$h(z) = C_p T(z) + gz + L_v q(z) \tag{3.28}$$

where z is the height, C_p being the specific heat of air, $T(z)$ the temperature of air at height z, g the acceleration due to gravity, L_v the latent heat of vaporization of water, and $q(z)$ the specific humidity at height z.

Given boundary condition values, the downdraft's originating mass flux can be defined as a function of the updraft mass flux at the originating level and the precipitation efficiency

Winter [2006]:

$$m_0 = \frac{\beta I_1 m_b}{I_2} \tag{3.29}$$

I_1 represents the normalized updraft condensation, I_2 the normalized downdraft evaporation, and β the fraction of the updraft condensation that reevaporates in the downdraft [Pal, 1997]. In addition, $(1 - \beta)$, the precipitation efficiency, is dependent on wind shear. Therefore, the Grell scheme simulates rainfall, R, as:

$$R = I_1 m_b (1 - \beta) \tag{3.30}$$

Heating and moistening in the Grell scheme is calculated from mass fluxes as well as detrainment at the top and bottom of the cloud [Pal, 1997]. Moreover, both the cooling effects of moist convective downdrafts as well as an upper limit on lateral mixing are included to avoid zero-order sources of error [Grell *et al.*, 1994].

As mentioned prior, due to the simplistic nature of the Grell scheme, two closure assumptions for the parameterization are available in RegCM3. Although in this study results presented are from the Grell scheme closed with the FC80 technique, simulations were performed with both closures.

The quasi-equilibrium Arakawa & Schubert method (AS74) is the default closing technique used in RegCM3. The AS74 closure assumes that the environment is stabilized by clouds at the same rate that it is destabilized by non-convective processes [Elguindi *et al.*, 2004]. This expression can be mathematically described as:

$$\frac{dABE}{dt} = \frac{dABE_{LS}}{dt} + \frac{dABE_{CU}}{dt} \approx 0 \tag{3.31}$$

where ABE is the available buoyant energy, LS is the subscript for large-scale, and CU is the subscript for cumulus convection [Pal, 1997]. Expressed as a mass flux, m_b, the

relationship is:

$$m_b = \frac{ABE'' - ABE}{NA\Delta t} \tag{3.32}$$

where, ABE'' is the buoyant energy generated by non-convective processes available for convection over the time period Δt and NA is the rate of change of AB per unit m_b.

As mentioned above, in this study, results presented with the Grell scheme implement the Fritsch and Chappell closure (FC80). This closure technique assumes that convection removes the available buoyant energy, ABE, over a given time scale as follows:

$$m_b = \frac{ABE}{NA\tau} \tag{3.33}$$

where τ is the ABE removal time scale

Designed to represent Type II or tropical convection (the most common form of convection) the AS74 closure assumption connects convective fluxes to tendencies in the atmospheric state. On the other hand, the FC80 closure technique, designed to model Type I or explosive convection which typically occurs at mid-latitudes, connects convective fluxes to instability in the atmosphere [Elguindi *et al.*, 2004]. In short, both closure schemes achieve statistical equilibrium between large-scale processes and convection.

3.5.3 Emanuel Scheme

The Emanuel scheme offers the newest cumulus convection option available to RegCM3. Triggered when the level of neutral buoyancy (LNB) is greater than the cloud base level (lifted condensation level-LCL), the scheme assumes that mixing in clouds is inhomogeneous and highly episodic as opposed to the continuous entraining plumes of such schemes as Grell and Kuo [Elguindi *et al.*, 2004]. Air parcels between these two levels are lifted where a fraction of the condensed moisture forms precipitation while the remaining fraction forms the cloud as shown in Figure 3-4. This resulting cloud is assumed to mix with

the surrounding environmental air according to a uniform spectrum of mixtures which descend or ascend to their respective LNBs [Emanuel, 1991]. Entrainment and detrainment rates of clouds and environmental air are functions of the vertical gradients of buoyancy found within the clouds [Elguindi *et al.*, 2004]. More specifically, the fraction of the total cloud base mass flux that mixes with its environment at a given level is proportional to the (undiluted) buoyancy rate of change with altitude [Emanuel, 1991].

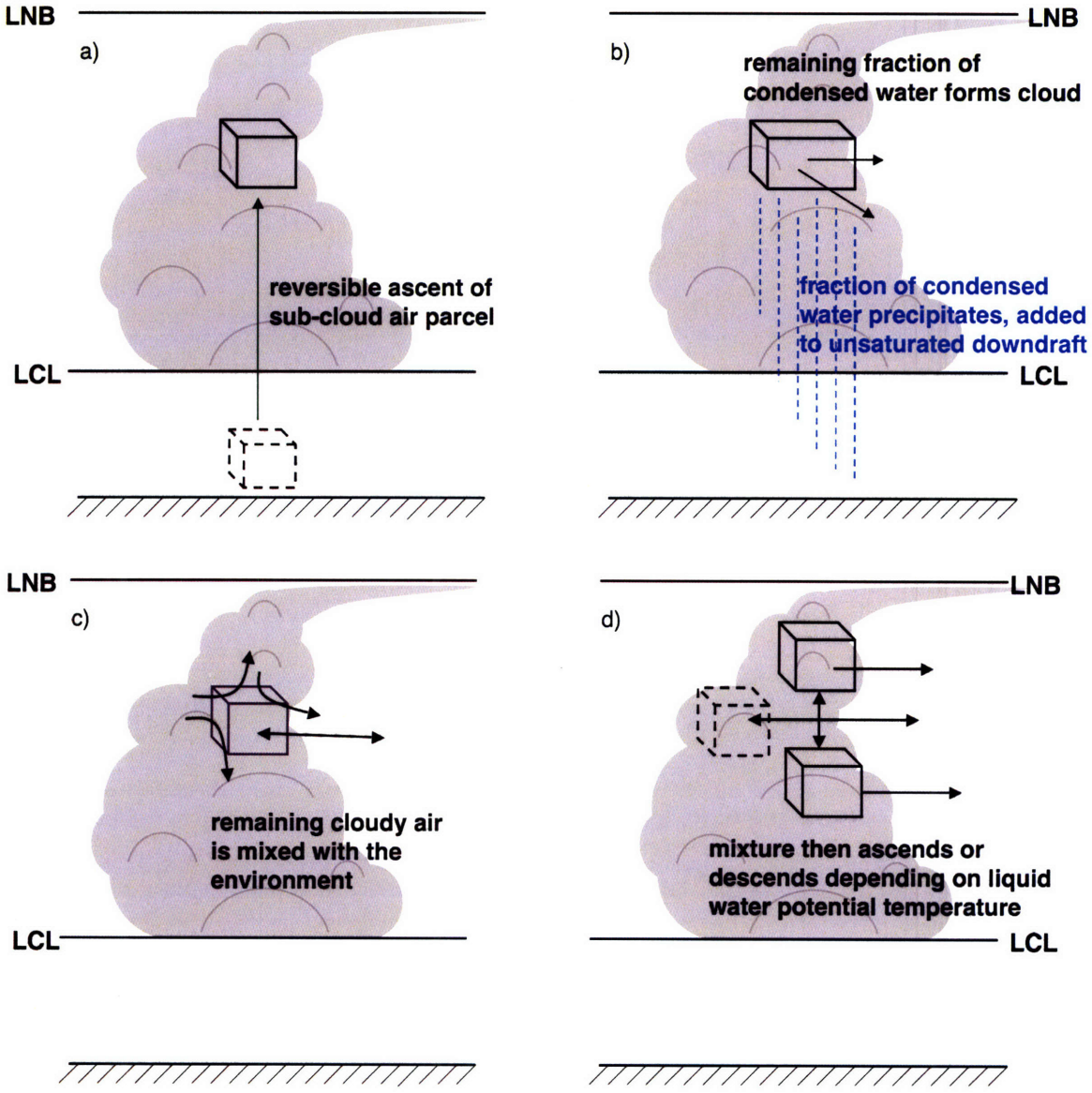

Figure 3-4: Schematic highlighting the fundamental processes of the Emanuel scheme adapted from Emanuel [1991]. Diagrams are labeled in order of the evolution of a typical, convectively active cloud parcel in the Emanuel scheme.

Since the Emanuel scheme is designed to represent the effects of all moist convection

(including shallow and even non-precipitating cumulus), the scheme is arguably the most physically realistic representation of convection offered in RegCM3. In addition, Emanuel offers a formulation for the auto-conversion of cloud water into precipitation. Likewise, ice processes are accounted for by permitting the auto-conversion water content threshold to be a function of temperature. Moreover, precipitation is added to a single, hydrostatic, unsaturated downdraft that can transport both water and heat to to the surrounding atmosphere [Elguindi *et al.*, 2004]. The Emanuel scheme also includes the transport of passive tracers within RegCM3. However, thorough testing of the scheme within RegCM3 has not been fully completed as of yet. For further information of the Emanuel scheme please refer to Emanuel [1991].

3.6 Large-Scale Precipitation Scheme

Large, resolvable-scale clouds and precipitation are calculated using the Subgrid Explicit Moisture Scheme (SUBEX) of Pal [2001]. Drawing from the work of Sundqvist *et al.* [1989], SUBEX relates the average grid cell relative humidity, rh, to the cloud fraction and cloud water found in the grid cell using the following relationship:

$$FC^{LS} = \sqrt{\frac{rh - rh_{min}}{rh_{max} - rh_{min}}} \tag{3.34}$$

where FC^{LS} is the fractional cloud cover, rh_{min} is the relative humidity threshold in which clouds begin to form, and rh_{max} is the relative humidity threshold at which the fractional cloud cover reaches unity [Pal, 2001]. If $rh \leq rh_{min}$, then FC^{LS} is assumed to be zero, and when $rh \geq rh_{max}$, FC^{LS} is assumed to be unity.

When cloud water Q_c^{LS} content breaches the autoconversion threshold Q_c^{th}, precipitation P^{LS} forms as such:

$$P^{LS} = C_{ppt}(Q_c^{LS}/FC^{LS} - Q_c^{th})FC^{LS} \tag{3.35}$$

where, C_{ppt} is the autoconversion rate. Conceptually, $1/C_{ppt}$ can be thought of as the characteristic time required for cloud droplets to convert into rain droplets. Once precipitation forms, it is assumed to fall instantaneously. Q_c^{th} is empirically derived from:

$$Q_c^{th} = C_{acs} 10^{-0.49+0.013T} \tag{3.36}$$

with, T, temperature in degrees Celsius and C_{acs} is the autoconversion scale factor, which accounts for the land or ocean based threshold that results from differences in density between land and ocean-based clouds.

In addition, SUBEX includes calculations for physically important precipitation processes such as raindrop accretion and evaporation. The representation of accreted cloud water from falling rain droplets follows the work of Beheng [1994], where the amount of accreted water, P_{acc}, is expressed as:

$$P_{acc} = C_{acc} Q_c^{LS} P_{sum} \tag{3.37}$$

with C_{acc} being the accretion rate coefficient and P_{sum} the accumulated large-scale precipitation from above falling through the cloud grid cell. In addition, evaporation from falling raindrops, a function of the ambient relative humidity, is accounted for using the formulation of Sundqvist *et al.* [1989] and will be elaborated upon in Chapter 4:

$$P_{evap} = C_{evap}(1 - rh) P_{sum}^{1/2} \tag{3.38}$$

Here, P_{evap} is the amount of evaporation and C_{evap} is a rate coefficient.

3.7 Ocean Flux Parameterization

For all simulations in this study, the Zeng ocean surface scheme is used within RegCM3. Therefore, for ocean cover in model runs, sensible heat SH, latent heat LH, and momentum τ fluxes are all approximated by the following bulk aerodynamic algorithms:

$$SH = -\rho_a C_{pa} u_* \theta_* \tag{3.39}$$

$$LH = -\rho_a L_v u_* q_* \tag{3.40}$$

$$\tau = \rho_a u_*^2 (u_x^2 + u_y^2)^{1/2} / u \tag{3.41}$$

where ρ_a is the air density, C_{pa} the specific heat of air, u_* is the frictional wind velocity, θ_* is the temperature scaling parameter, L_v is the latent heat of vaporization of water, q_* is the specific humidity scaling parameter, u_x is the mean zonal wind component, u_y is the mean meridional wind component, and u is wind speed [Elguindi *et al.*, 2004]. For a more rigorous description of the Zeng ocean scheme please refer to Zeng *et al.* [1998].

3.8 BATS1e

Dickinson *et al.*'s land surface model, Biosphere-Atmosphere Transfer Scheme 1e (BATS1e), offers a comprehensive representation of the physics that drive land surface processes. BATS1e can be run offline, or coupled to a RCM/GCM, as it is coupled to RegCM3 in these experiments [Dickinson *et al.*, 1993]. For a full list of the parameter values used in BATS1e please refer to table provided in Appendix A.1. The overall structure of BATS1e is shown in Figure 3-5. Seven primary tasks are performed by the land surface scheme,

their relevant equations can be found in Appendix A.

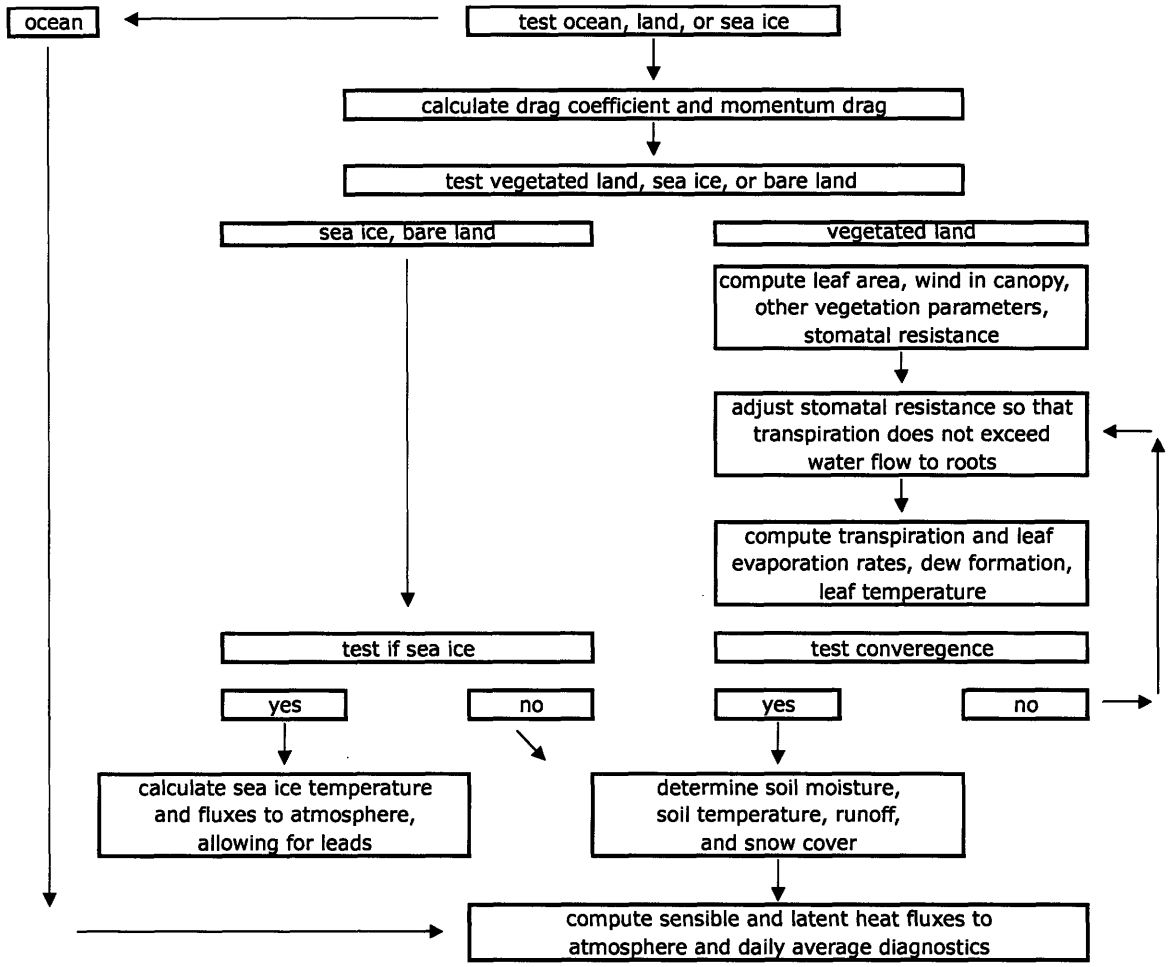

Figure 3-5: Flow chart for Biosphere-Atmosphere Transfer Scheme version 1e (BATS1e) [Dickinson *et al.*, 1993].

To begin with, the first function of BATS1e is assigning both vegetation and soil characteristics for each grid cell in the model. Available in 2, 3, 5, 10, 30, and 60 minute resolutions, the United States Geological Survey's (USGS) Global Land Cover Characterization (GLCC) dataset is used to assign the vegetation type for each grid cell [United States Geological Survey, 1997]. It is important to note that vegetation type dictates the soil characteristics for a given grid cell in BATS. For example, a desert grid point, as seen in some gridboxes for experiments over Kuwait, would be assigned a coarse, sandy soil.

Next, BATS calculates the albedo for sea ice, bare soil ,and vegetated lands. The albedo is a a function of multiple surface characteristics [e.g. soil type, soil moisture, and sun an-

Land Cover	Vegetation Class	Vegetation albedo wavelengths < 0.7μm	Vegetation albedo wavelengths < 0.7μm
Crop/Mixed Farming	1	0.10	0.30
Short Grass	2	0.10	0.30
Evergreen Needleleaf Tree	3	0.05	0.23
Deciduous Needleleaf Tree	4	0.05	0.23
Deciduous Broadleaf Tree	5	0.08	0.28
Evergreen Broadleaf Tree	6	0.04	0.20
Tall Grass	7	0.08	0.30
Desert	8	0.20	0.40
Tundra	9	0.10	0.30
Irrigated Crop	10	0.08	0.28
Semi-Desert	11	0.17	0.34
Ice Cap/Glacier	12	0.80	0.60
Bog/Marsh	13	0.06	0.18
Inland Water	14	0.07	0.20
Ocean	15	0.07	0.20
Evergreen Shrub	16	0.05	0.23
Deciduous Shrub	17	0.08	0.28
Mixed Woodland	18	0.06	0.24
Forest/Field Mosaic	19	0.06	0.18
Water and Land Mixture	20	0.06	0.18

Table 3.1: BATS1e vegetation types [Winter, 2006].

gle] (refer to Appendix A.1). The albedo of a vegetated surface is determined by the vegetation type (see Table 3.1), with albedos for each vegetation drawn from multiple studies, but mainly Monteith [1976].

Calculation of the surface drag coefficient C_D, is the third major set of computations that BATS1e must perform. Please refer to Appendix A.2 and A.3 for equations used to calculate surface drag coefficients.

The fourth set of tasks performed by BATS1e includes all plant water budget calculations [e.g. foliage and stem water fluxes, resistance (stomatal and water induced) limited transpiration, and precipitation interception] [Dickinson *et al.*, 1993]. A more thorough description of these processes can be found in Appendix A.4 and A.5.

Calculated in the fifth set of BATS equations, transpiration, E_{tr}, is determined using a similar scheme to the one-layer formulation credited to Monteith [Thom and Oliver, 1977]. Major differences between Dickinson *et al.*'s formulation and Monteith's include having a partially wetted canopy, as well as explicitly separate equations/resistances for energy fluxes between foliage and air within the canopy, or between air within the canopy and air above the canopy [Winter, 2006].

Once transpiration is calculated (Appendix A.6), the foliage temperature is solved for

iteratively and mainly a function of heat and moisture transport within the canopy [Dickinson *et al.*, 1993].

Task six involves computing soil, snow, or sea ice surface temperatures dependent on radiation inputs, soil/snow heat capacity, and thermal conductivity [Dickinson *et al.*, 1993]. An example of such calculations is provided in Appendix A.7.

Lastly, soil moisture is determined by evaporation as well as surface and groundwater runoff. In BATS1e, the soil profile contains three layers: a 10 cm surface soil layer, a 1 to 2 m root layer, and a 3 m deep soil layer [Pal *et al.*, 2000]. Once water is applied to the soil surface through either snowmelt or rainfall, it is partitioned to either runoff or infiltration, and then permitted to move between the three layers based mainly on vegetation and soil properties [Dickinson *et al.*, 1993]. In addition, evaporation from the soil is modeled as function of the aerodynamic characteristics of both the soil surface and the soil conductivity [Dickinson *et al.*, 1993]. The partitioning of runoff and infiltration is primarily a function of soil moisture where little runoff will occur from soils at field capacity. Therefore, nearly all water is sent to runoff from saturated soils [Dickinson *et al.*, 1993]. Refer to Appendix A.8 and A.9 for BATS1e equations for infiltration and runoff.

3.9 RegCM3 Datasets

Four different reanalysis datasets are available for use as initial and boundary conditions in RegCM3: the National Centers for Environmental Prediction (NCEP) reanalysis 1 dataset (NNRP1) [Kalnay *et al.*, 1996], the NCEP reanalysis 2 dataset (NNRP2) [Ebisuzaki, 2005], the European Centre for Medium-Range Weather Forecasting (ECMWF) reanalysis dataset [European Centre for Medium-Range Weather Forecasts, 1995], and the ECMWF 40-year reanalysis (ERA40) dataset [Uppala *et al.*, 2005]. In addition, output from a number of GCMs may also be used to drive the boundaries of RegCM3. For baseline experiments performed in this study (i.e. Sections 4.1.1 & 4.1.2), NNRP2 lateral boundary conditions (LBCs) are used. However, further simulations with ERA40 LBCs are performed in Section 4.4.2.

Due to RegCM3's lack of an interactive ocean model, sea surface temperatures, (SSTs)

are prescribed by the National Oceanic and Atmospheric Administration (NOAA) Optimum Interpolation Sea Surface Temperature (OISST) dataset [Reynolds *et al.*, 2002] or the Hadley Centre Meteorological Office Global Sea Surface Temperature (GISST) dataset [Rayner *et al.*, 1996]. Please refer to Chapter 4 for a detailed description of datasets used for experiments in this study.

Finally, two land surface datasets are used to initialize RegCM3. The first, topography, is derived from elevations provided in the United States Geological Survey's (USGS) Global 30 arc second elevation dataset (GTOPO30) [United States Geological Survey, 1996]. As mentioned prior, land cover is given by the USGS GLCC dataset [United States Geological Survey, 1997]. While GTOPO30 and GLCC have spatial resolutions of 30 arc seconds and 1 km respectively, both are used in 2, 3, 5, 10, 30, or 60 minute resolutions [Winter, 2006].

Chapter 4

Modeling the Hydroclimatology of Kuwait

If examining the effects of anthropogenic forcings on Kuwait's climate is desired, it is first necessary to simulate accurately the natural climate variability of the country. This chapter examines using a RCM to simulate the climate of Kuwait namely addressing the overestimation of rainfall simulated by RegCM3 over the region. Modifications are made to the model to include sub-cloud layer evaporation in the Kuo convection scheme as well as improving sub-cloud evaporation in the large scale precipitation routine. In addition, an examination of domain choice, convection scheme, and boundary conditions implemented are discussed. Results indicate a significant improvement in RegCM3's ability to simulate the hydroclimatology of Kuwait.

4.1 Model Setup Selections

4.1.1 Domain Choice

Much experimentation was performed with domain size, nesting, and resolution within RegCM3. All results presented in this section use NCEP reanalysis 2 (NNRP2) data for initial and boundary conditions as well as NOAA's OISST's unless otherwise stated. Initial runs of 10 km resolution centered over Kuwait produce unrealistic precipitation patterns

and therefore it is necessary to expand the model's domain while running RegCM3 at a coarser horizontal resolution.

As a result, further work entailed implementing one way nesting within RegCM3. That is, model output from a coarser, outter domain is used to drive the initial and boundary conditions of simulations of an inner, finer resolution domain. One way nesting offers more accurate spatial distributions of rainfall, yet it fails to capture the magnitude of rainfall adequately over the region.

Therefore, it was decided that in order to simulate Kuwait's rainfall properly, the model domain must cover a significant portion of the Middle East and eastern Mediterranean Sea, where mid-latitude synoptic systems form and then traverse south towards Kuwait. As seen by comparing Figure 4-1a & 4-1c, a larger domain does significantly better in capturing the spatial distribution as well as the magnitude of rainfall over the Arabian Gulf region. This domain was then run at 30 km resolution (shown in Figure 4-1b) and results deteriorated as rainfall over the region was further overestimated by the finer resolution.

4.1.2 Precipitation & Convection Schemes

In addition to the extensive work done with domain setup, many experiments were completed in varying parameters of both large scale and convective precipitation schemes in RegCM3. Results indicated that altering parameters, [e.g. cloud relative humidity thresholds, auto conversion scale factors] in the large scale precipitation scheme does not significantly affect precipitation patterns or magnitudes over our domain. However, the model results over the domain are particularly sensitive to the implemented convection scheme. This study finds that the Kuo scheme does best in simulating not only the spatial distribution but also the magnitude of precipitation over the area of interest (Figure 4-2). More specifically, the Emanuel scheme, which was physically modeled for tropical climates, does not accurately capture the spatial distribution of rainfall as described by CRU (compare Figure 4-2a & 4-2c). Other schemes, such as the Grell (FC80 closure) which was designed for explosive convection typical in the Midwest of America, greatly overestimates annual rainfall over the entire Arabian Peninsula. For example, in simulations using the Grell scheme

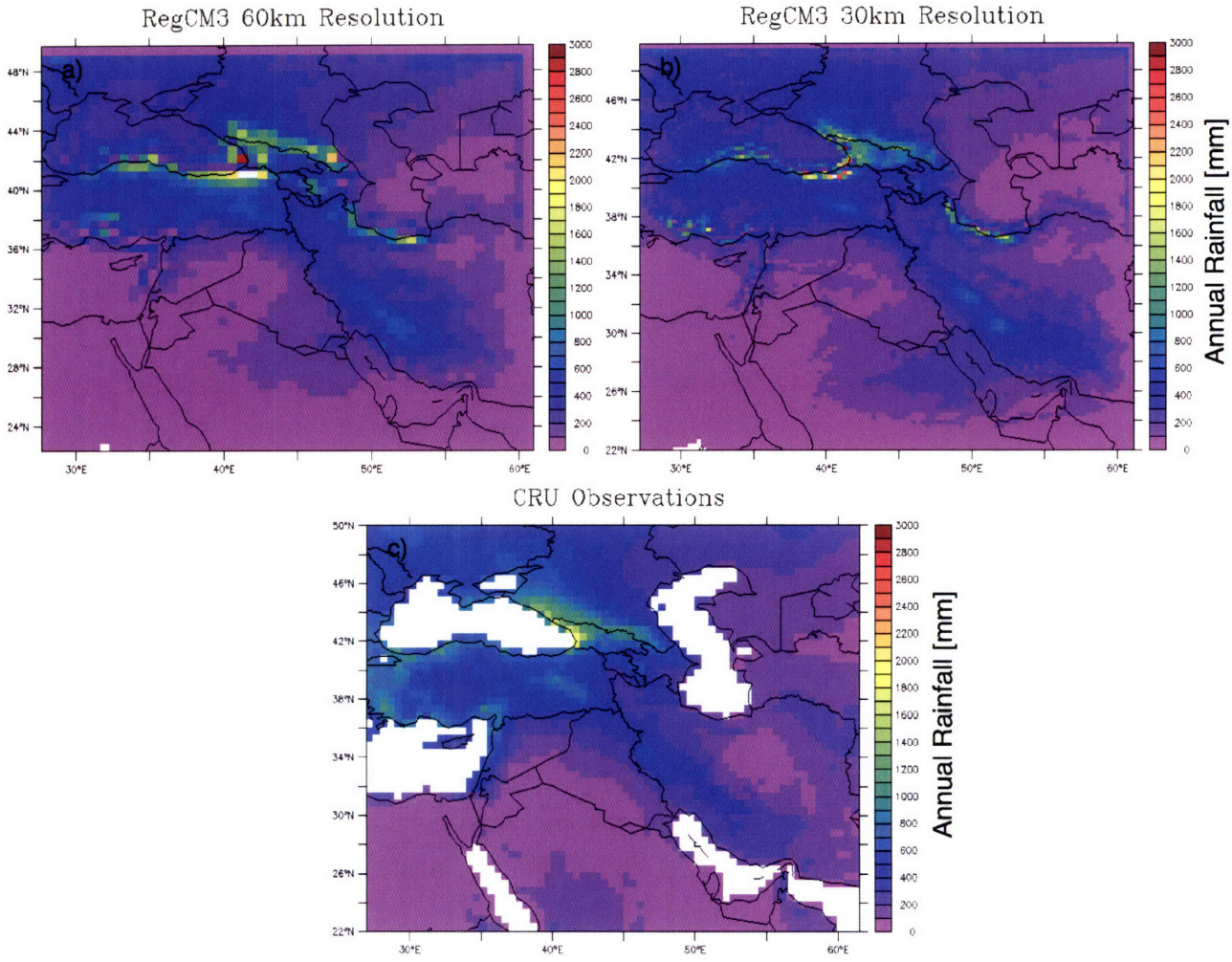

Figure 4-1: Expanded domain results for Middle East annual precipitation (mm) for the period from 1996 to 2000 in a) RegCM3 at 60 km resolution, b) RegCM3 at 30 km resolution, and c) CRU observations. Note all model physics are held constant in both model simulations, except resolution.

(Figure 4-2d), annual rainfall totals in Kuwait are simulated well over 300 mm while observational estimates are much closer to 110 mm. Likewise, using the Grell scheme with the AS74 closure (modeled for tropical convection) yielded similar overestimations. Lastly, since the Kuo simulations (Figure 4-2b) most accurately capture the magnitude and spatial distribution of rainfall over Kuwait, it is used in all further simulations in this study.

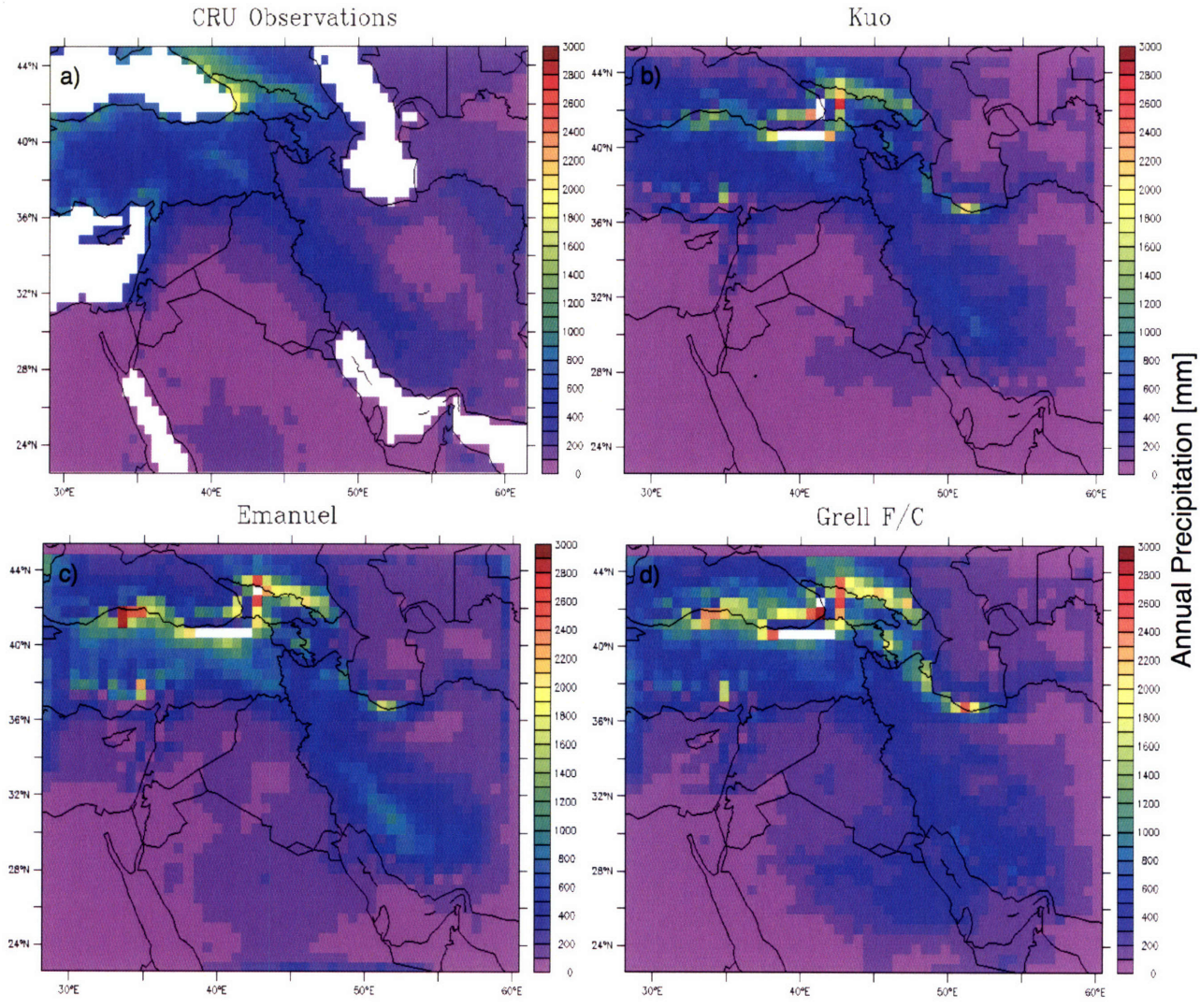

Figure 4-2: Middle East annual precipitation (mm) for the period from 1996 to 2000 in a) CRU observations, b) RegCM3 with Kuo, c) RegCM3 with Emanuel, and d) RegCM3 with Grell (Fritsch and Chappell closure—FC80). Note all other model physics are held constant in model simulations, except for the noted convection schemes.

4.2 Model Improvements

4.2.1 Large Scale Sub-cloud Evaporation-SUBEX

Since a focus of this chapter is improving SUBEX's raindrop evaporation, a brief summary of precipitation formulation in the scheme is provided. RegCM3's large scale rainfall evaporation is modified by improving the representation of the evaporation rate coefficient.

SUBEX dramatically improves RegCM3's representation of clouds, rainfall, and the energy budget [Pal *et al.*, 2000]. Following the work of Pal *et al.* [2000], large scale rainfall, P^{LS}, forms in RegCM3 once cloud water content ,Q_c^{LS}, breaches the autoconversion threshold, Q_c^{th}, as follows:

$$P^{LS} = C_{ppt}\left(\frac{Q_c^{LS}}{FC^{LS}} - Q_c^{th}\right) FC^{LS} \qquad (kg * kg^{-1}s^{-1}) \tag{4.1}$$

where, FC^{LS} is the fraction of the grid cell covered by clouds, which is a function of the average relative humidity of the gridcell [Sundqvist *et al.*, 1989]. C_{ppt} (s^{-1}) is the inverse of the characteristic time it takes cloud droplets to convert into raindrops, the autoconversion rate. The cloud water threshold (Q_c^{th},) with units of kg_{water} per kg_{air}, is described by an empirical function of temperature. In addition, the scheme accounts for raindrop accretion which was previously excluded from RegCM3's explicit moisture scheme. As formulated in the work of Sundqvist *et al.* [1989], raindrop evaporation, which occurs in the cloud free portion of the gridcell, is modeled as such:

$$P_{k,evap} = C_{evap}(1 - rh)\sqrt{P_{sum,k}} \qquad (kg * kg^{-1}s^{-1}) \tag{4.2}$$

where rh is the ambient relative humidity. P_{sum}, with units of $kg{*}m^{-2}s^{-1}$, is the large-scale precpitation falling from above and is uniformly distributed across the gridbox. The evaporation rate coefficient, C_{evap}, the focus of the improvement proposed in this study, will be referred to as the static evaporation coefficient. The moisture and heat tendencies are updated for each layer to account for the amount of rainwater evaporated within that layer. Thus, rainfall leaving a gridcell at vertical level k (where k increases as one moves

toward the surface) is simply:

$$P_k^{LS} = P_{k-1}^{LS} - P_{k,evap} \qquad (kg * kg^{-1}s^{-1}) \tag{4.3}$$

$$\text{and,} \qquad P_{sum,k} = P_{k-1}^{LS} \tag{4.4}$$

Following the work of Georgakakos and Bras [1984] in their formulation of rainfall evaporation in a hydrological station model, SUBEX's C_{evap} is scaled to account for the variability of water vapor diffusivity as a function of the model layer's temperature and pressure. The diffusion coefficient's assumed form of dependence on temperature and pressure is based on the empirical analysis of Pruppacher and Klett [1978]. Thus, the new rate coefficient, which will be referred to throughout as the dynamic evaporation coefficient, is:

$$C_{evap}{}' = C_{evap}\left(\frac{T_o}{T^*}\right)^{1.94}\left(\frac{P^*}{P_o}\right) \qquad (kg * m^{-2}s^{-1})^{-1/2}s^{-1} \tag{4.5}$$

where P^* & T^* take values of 1013.25 mb and 273.15 K, respectively and P_o & T_o are values for each atmospheric layer. For a typical winter day (when most large scale rainfall occurs in Kuwait) surface temperatures are about 25°C and surface pressure reaches approximately 1000 mb [Al Kulaib, 1984]. As a result, evaporation in lower model layers can increase by more than 20% with the new dynamic coefficient of evaporation. Table 4.1 provides all prescribed constant SUBEX parameters used in these simulations.

Parameter	Value	Units
Auto-conversion rate C_{ppt}	5 x 10^{-4}	s^{-1}
Auto-conversion scale factor C_{acs}	4 x 10^{-1}	—
Accretion rate C_{acc}	6.0	$m^3 * kg^{-1}s^{-1}$
Static coefficient of evaporation C_{evap}	2 x 10^{-5}	$(kg * m^{-2}s^{-1})^{-1/2}s^{-1}$

Table 4.1: Summary of SUBEX constants used.

4.2.2 Convective Sub-cloud Evaporation: Kuo Scheme

As mentioned by Sundqvist *et al.* [1989], most convection schemes lack sub-cloud evaporation since it is assumed that rain falls through almost saturated air. However, in semi-arid

climates this is not the case. Studies have shown that in these regions between 25% and 50% of convective rainfall can evaporate before reaching the ground (depending on rainfall intensity and cloud base height [Rosenfeld and Mintz, 1988]). Further work by Al Kulaib [1984] describes many accounts in which such convective activity occurs over Kuwait with rainfall totals less than 5 mm. As a result, to simulate accurately Kuwait's rainfall, it is necessary to add a sub-cloud convective evaporation scheme. Modeled after SUBEX's layer by layer approach for evaporation, the method applied here may also be adopted to other convection schemes. As mentioned prior, Kuo's convective parameterization is used in these experiments because of its superior performance over our domain. As mentioned in Chapter 3, the Kuo scheme implements a simple integrated column approach in representing convective rainfall which is triggered by both a convectively unstable vertical sounding and large scale moisture convergence [Kuo, 1974]. Rainfall in the Kuo scheme is calculated from the following equation:

$$P_o^{CU} = M_t(1-\beta) \tag{4.6}$$

where, M_t is the vertically integrated moisture convergence described by

$$M_t = \left(\frac{m^2}{g}\right)\int_0^1 \frac{\nabla p^* s \dot{V} q_v}{m} d\sigma \tag{4.7}$$

where m is the mass flux, g is acceleration due to gravity, ∇p^* is a function of surface and top of model pressure, $\dot{V}$ is dependent on horizontal velocity, q_v is the mixing ratio of water vapor, and σ is the vertical sigma level. The term β, the rainfall efficiency, is determined by the average relative humidity of the sounding $\overline{RH}$ as follows:

$$\beta = 2 * (1 - \overline{RH}) \quad \text{for,} \quad \overline{RH} \geq 0.5 \quad \text{otherwise,} \quad \beta = 1 \tag{4.8}$$

Similar to SUBEX evaporation, rainfall evaporation is allowed from the model's cloud-base level down to the surface as calculated in Equation 4.2 while using the dynamic coefficient of evaporation of Equation 4.5. Because rainfall in the Kuo scheme is calculated in a column integrated approach, it is assumed that P_o^{CU} is the total rainfall at the cloud-base

level as calculated in Equation 4.6. Then, evaporation is permitted to occur layer by layer from this initial amount as follows:

$$P_k^{CU} = P_o^{CU} - P_{k,evap} \quad where, k = cloudbase \tag{4.9}$$

and,

$$P_{k+1}^{CU} = P_k^{CU} - P_{k+1,evap} \tag{4.10}$$

where,

$$P_{k+1,evap} = C'_{evap}(1 - rh)\sqrt{P_k^{CU}} \tag{4.11}$$

and so forth from k = cloud-base down to $k + 1$= surface. Again, it is important to note that moisture and heat tendencies are updated for each layer to account for water evaporated in that layer. Figure 4-3 provides a schematic of the sub-cloud layer evaporation added to the Kuo scheme.

4.3 Experiment Design

Simulations using RegCM3 were completed spanning the period from 1982 to 2002. Afterwards, longer simulations (1972-2002) were performed and results are found to be similar to the twenty year runs. Therefore, results presented are from simulations spanning for twenty years. The domain, centered at 33.5°N, 44°E at 60 km resolution, has 52 points in the zonal and meridional direction using a Lambert Conformal projection. Thus, the domain covers most of the Middle East from the Black and Aral Seas in the North to the southern Red Sea in the SW and Oman in the SE. Figure 4-4 represents the model domain as well as topography and land use in the simulations. Two different sets of initial and boundary conditions are implemented and examined: NNRP2 of Kalnay *et al.* [1996] and ERA40. Lateral boundary conditions were enforced by applying the exponential relaxation of Davies and Turner [1977]. As mentioned prior, SST's are prescribed to RegCM3 from the National Oceanic and Atmospheric Administration (NOAA) Optimally Interpolated Sea Surface Temperatures (OISST) dataset which has a temporal coverage from 1982

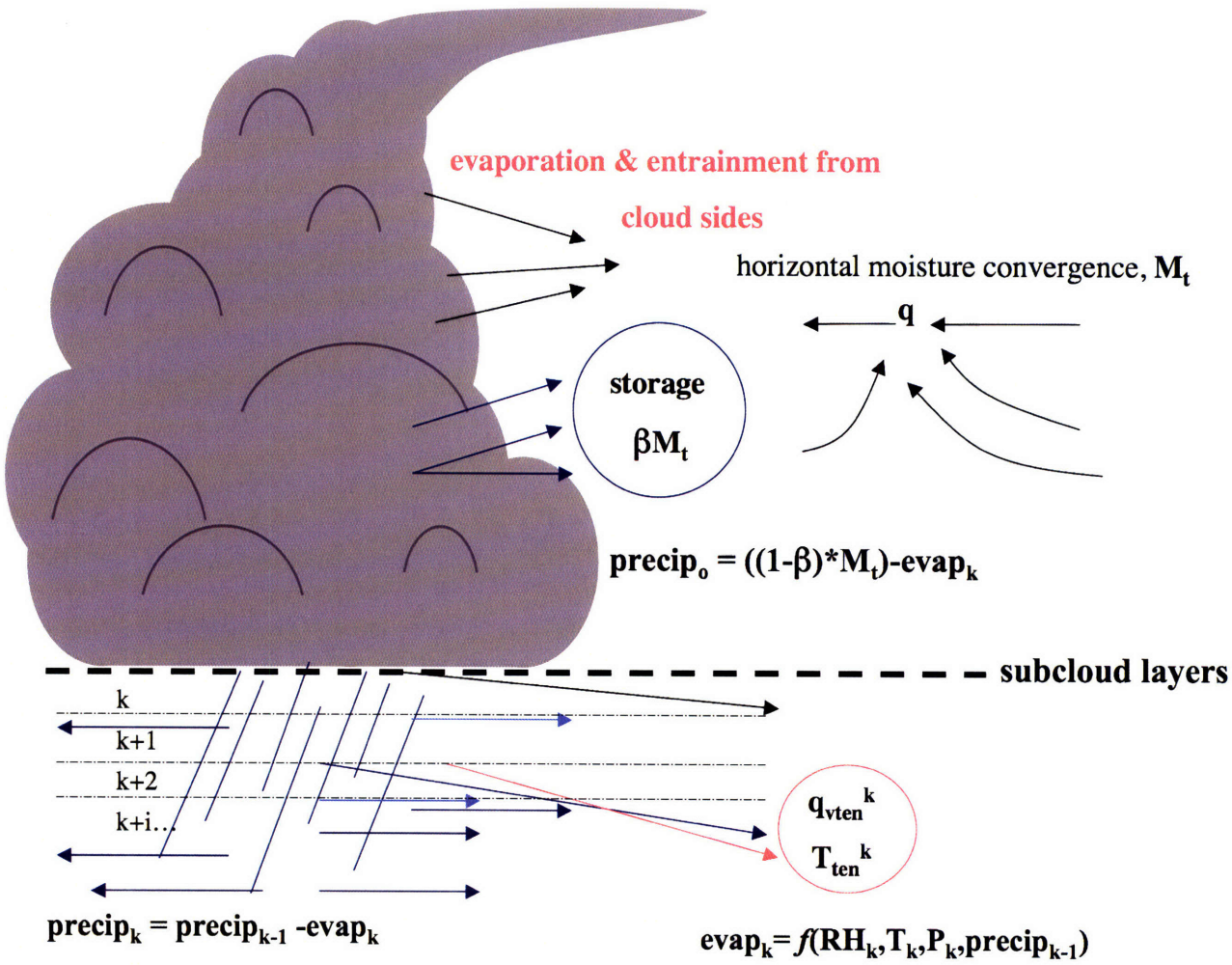

Figure 4-3: Diagram showing modifications made to sub-cloud layers in the Kuo convection scheme.

to 2002 [Reynolds, 2002]. The SST datasets are 1° x 1° weekly resolution and are based on in situ and satellite observations.

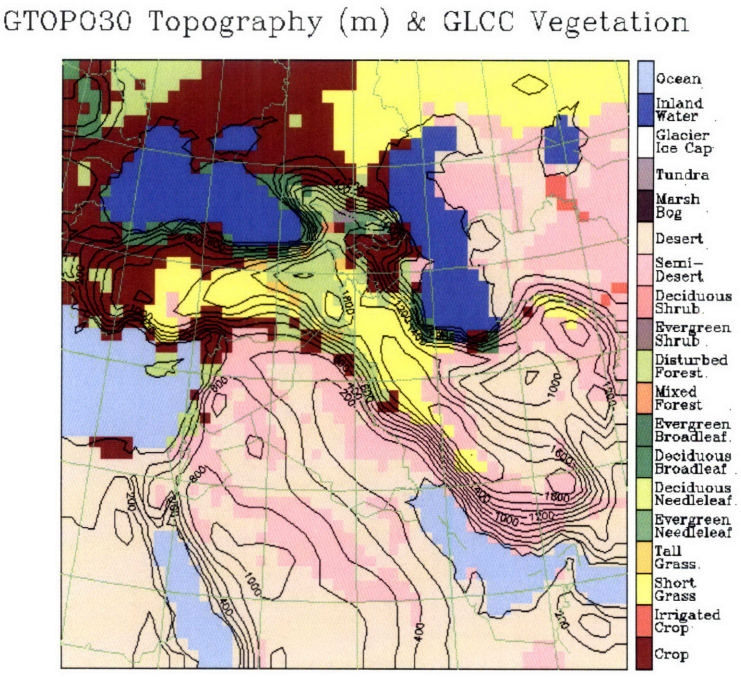

Figure 4-4: Domain implemented for all simulations with topography contoured (200m intervals) and vegetation shaded. Kuwait is classified by semi-desert and desert land cover.

To account for the local effects of LBC's on model results, three degrees along each boundary of the model's output are not analyzed. Nonetheless, results here focus mostly on model output from 28.4°N to 30.2°N and from 46.5°E to 48.5°E (the approximate location of Kuwait), which should be free from most LBC influences. Table 4.2 provides a summary of the simulations completed, the name prescribed to each experiment, and the datasets used in each simulation.

Run	Years	LBC	Evaporation	SST
NCEP	1982-2002	NNRP2	—	OISST
ECMW	1982-2002	ERA40	—	OISST
EEVP	1982-2002	ERA40	Kuo + SUBEX	OISST

Table 4.2: Summary of simulations with parameters varied. Names given are used to reference each simulation in the text.

4.4 Results and Discussion

Several studies utilizing RegCM3 to model arid regions have compared model output to re-analysis and observational data. For example, Small *et al.* [1999] have shown that general circulation patterns [i.e. 500 mb geopotential heights and 500 mb winds] are well represented by RegCM over a similar domain in central Asia. In addition, Evans *et al.* [2002] have used RegCM to model the climate of the Middle East in a domain similar to that of this study. Their results show reasonable temperature representation in the model with a slight cool bias in winter (December, January, February-DJF). Similarly, we find a cool bias (of around one degree) over the entire domain. However, summer (June, July, August-JJA) average temperatures show a significant warm bias (see Figure 4-5). This summer warm bias is currently being addressed and results will be reported in the near future.

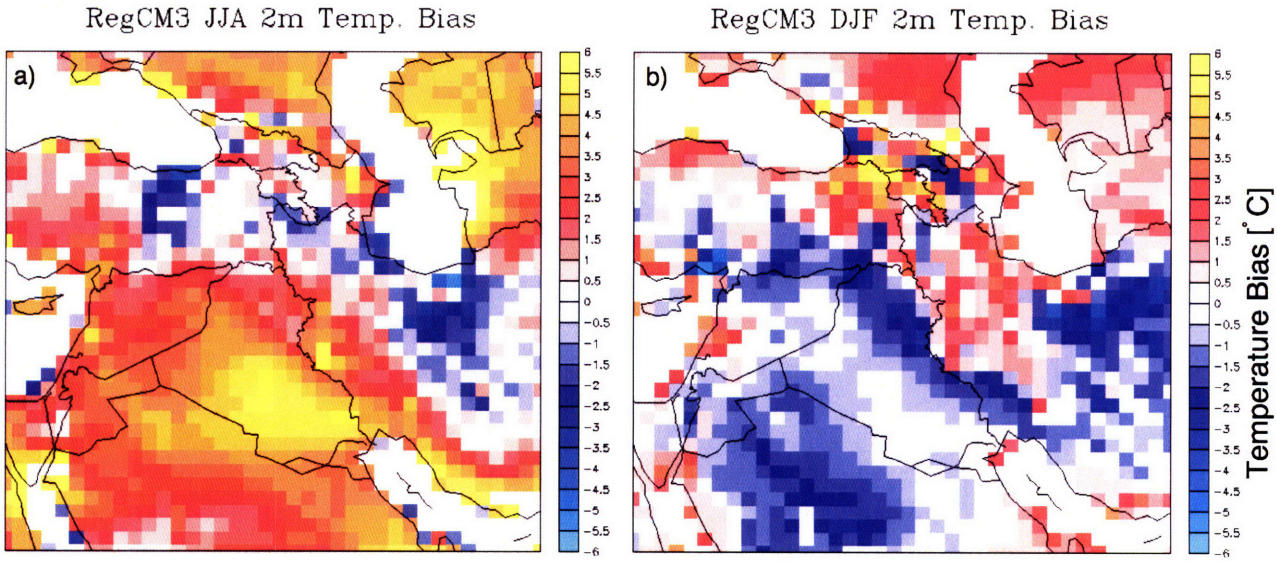

Figure 4-5: Temperature bias between RegCM3 simulation and CRU observations for two meter temperatures in a) summer (JJA) and b) winter (DJF).

4.4.1 Model Validation

For baseline model performance, a comparison of both NCEP & ECMW simulations of annual rainfall to CRU observations is made. To begin with, both simulations significantly

overestimate Kuwait's annual rainfall, which CRU estimates at 110 mm. More specifically, shown in Table 4.3, NCEP over-predicts annual totals by over 40% at 154 mm per year while ECMW predicts 148 mm which is 35% too large. These values are still somewhat better than rainfall in reanalysis datasets such as NNRP2 and ERA40 which severely underestimate rainfall at 50 mm and 75 mm per year, respectively. Nevertheless, when comparing CRU's (Figure 4-6a) annual rainfall to Figures 4-6b & 4-6c (NCEP & ECMW), RegCM3 does well in simulating the spatial distribution of precipitation over the domain. For example, the model correctly simulates the gradient of rainfall from Kuwait to the Zagros mountains of western Iran. However, attention should be paid to the extensive, excessive, wet tongue of rainfall that extends from central Saudi Arabia to the Persian Gulf. This area is clearly seen in Figures 4-7a & 4-7b which display the annual difference between CRU and RegCM3 rainfall. Some locations in this southern region have annual rainfall overestimated by more than 60 mm, which is nearly double the yearly rainfall (see Figure 4-7c). The neglect of sub-cloud layer evaporation most likely contributes to these results; therefore, addressing this problem should help reduce simulated values in the region. Additionally, in both NCEP & ECMW, rainfall over the Zagros mountains is over-estimated by nearly 300 mm or 75% more than observations as seen in Figure 4-7c & 4-7d. On a similar note, the spatial distribution of rainfall across the Black Sea near Turkey and the Caspian Sea adjacent Iran are modeled correctly but with magnitudes significantly overestimated. This amplification is caused by steep topography gradients that exist along the coastline of the Black and Caspian seas where the Koroglu, Caucasus, and Elburz mountain ranges are located respectively. With winds blowing onshore over topography of one kilometer and higher, orographic lifting occurs with a constant, abundant supply of moisture which excessively precipitates out. The dry bias in RegCM3 along the eastern Mediterranean Coast and western Saudi Arabia is most likely a result of model resolution. That is, at 60 kilometers, RegCM3 does not capture the finer scale mountainous topography that enhances rainfall totals in both areas. Lastly, analysis reveals that RegCM3 correctly simulates the seasonal cycle of Kuwait rainfall, where the rainy season begins in November and ceases in April (Figure 4-8a). In addition, when compared to TRMM daily rainfall values, the model does well in simulating finer temporal rainfall events (see Figure 4-8b).

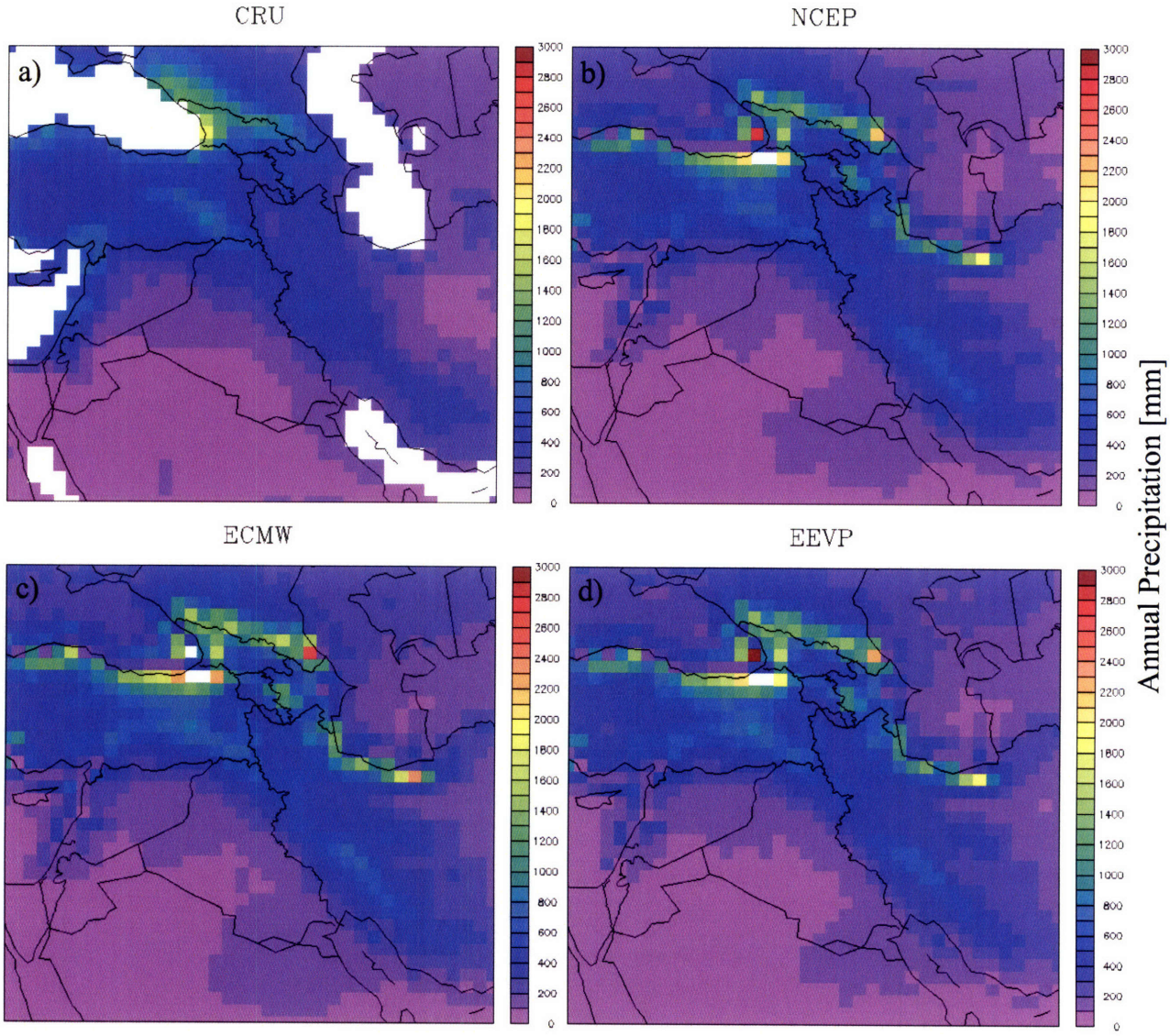

Figure 4-6: Average annual rainfall (in mm) from 1982-2002 for a) CRU observations b) NCEP simulation c) ECMW simulation d) EEVP simulation.

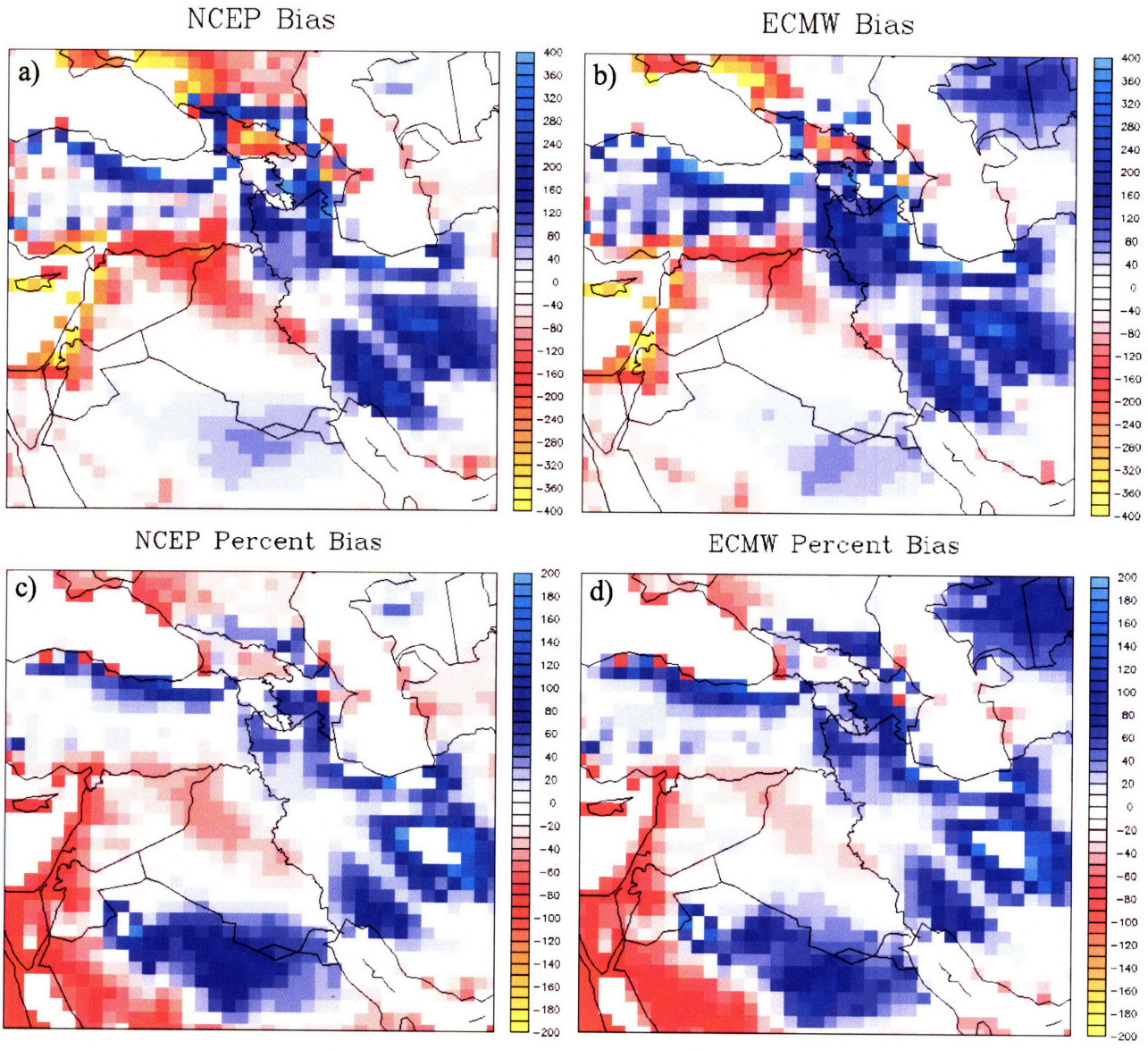

Figure 4-7: Total annual precipitation difference (mm) between CRU and a) NCEP b) ECMW simulations for 1982-2002 period. Percent bias between CRU and c) NCEP d) ECMW. Red shaded (positive) areas indicate locations where model results are drier than observations, blue shaded (negative values) indicate locations where model results are wetter than CRU observations.

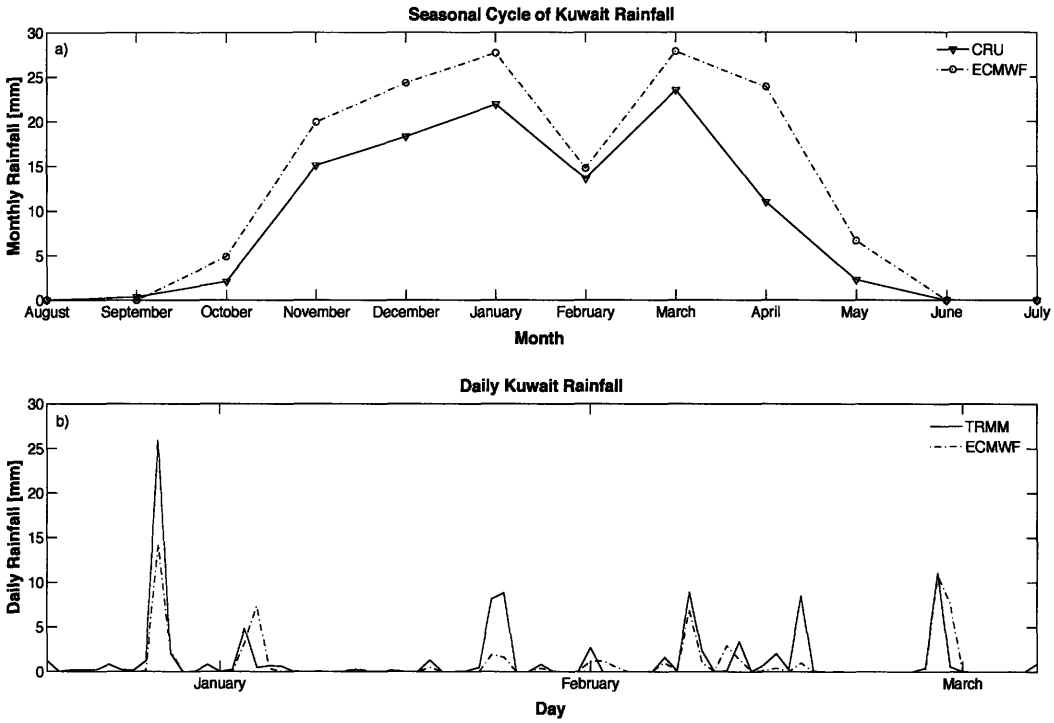

Figure 4-8: Temporal plot of Kuwait a) average monthly rainfall (mm) for period of 1982-2002 for CRU and ECMW simulation and b) daily rainfall (mm) from January, 1999 to March, 1999 for TRMM and ECMW simulation.

	Kuwait - Country			Kuwait City Airport		
	μ [mm]	σ [mm]	C_v	μ [mm]	σ [mm]	C_v
CRU	110	35	0.32	100	40	0.39
WMO	—	—	—	112	74	0.66
GPCP	188	81	0.43	182	93	0.51
NCEP	154	119	0.77	162	147	0.91
ECMW	148	101	0.68	143	113	0.79
EEVP	126	88	0.71	122	106	0.87

Table 4.3: Summary of observations and simulation results for country of Kuwait and Kuwait City International Airport. Mean (μ) annual rainfall in mm, yearly standard deviation (σ) in mm, and the coefficient of variation C_v are presented.

4.4.2 Effects of Boundary Conditions

Figures 4-6 & 4-6 indicate that boundary conditions have very little effect on RegCM3's spatial distribution(or magnitude) of Kuwait rainfall. The similarities are more apparent in Figures 4-9a & 4-9b which display the total and percent differences between NCEP & ECMW annual precipitation. Yearly differences between the two simulations for Kuwait are 6 mm and 4% respectively. However, as seen in Figure 4-9a, ECMW possesses significantly wetter annual rainfall in the northern portion of the domain. This increased precipitation is approximately 10 to 20% more than NCEP results (Figure 4-9b). As a result, ECMW output is closer to CRU observations in northern Turkey and Georgia as exhibited in Figure 4-7b. This pattern is most likely due to ERA40 transporting more moisture at the boundaries than NNRP2. As a result, more rainfall occurs along this inflow boundary. In addition, ECMW is somewhat drier than NCEP in western Saudi Arabia (Figure 4-9b). However, the actual difference in precipitation, Figure 4-9a, is less than 10 mm and hence essentially insignificant.

Comparison to CRU

RegCM3 results show substantial differences in interannual variability compared to measured values (see Table 4.3). For example, the NCEP simulation exhibits large year to year variation in rainfall. Compared to CRU's yearly standard deviation of 35 mm, NCEP's value of 119 mm is nearly 2.5 times larger than observations. It should be noted that signif-

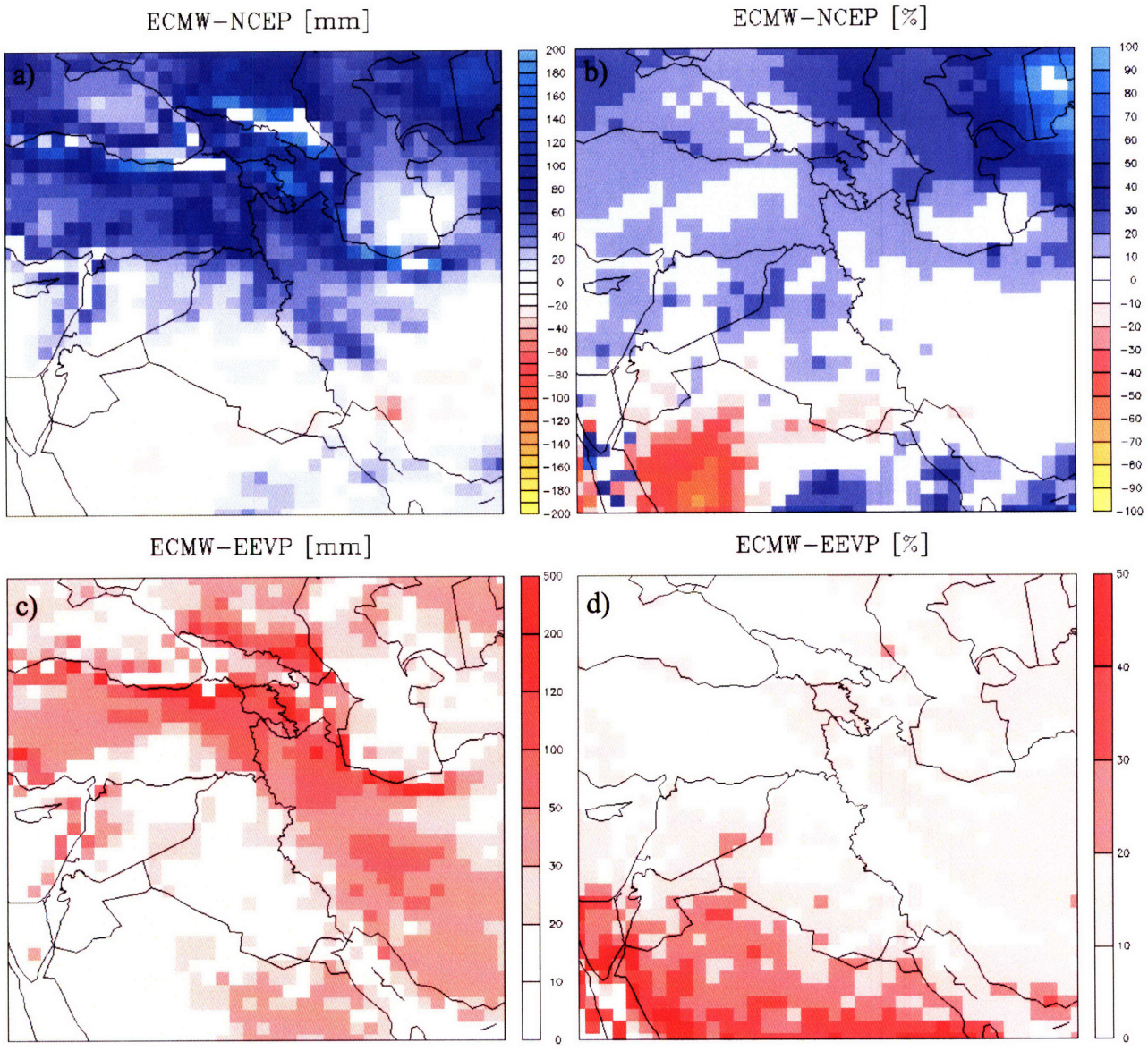

Figure 4-9: Annual precipitation difference between ECMW and NCEP simulations highlighting boundary condition effects in a) total annual difference (mm) and b) percent difference. Also shown are annual precipitation differences between ECMW and EEVP highlighting effects of evaporation changes in c) total annual difference (mm) and d) percent difference.

icant smoothing does occur in CRU estimates, which accounts for the eight closest station observations in calculating each gridbox's value. However, such large interannual variability reveals the model's inability to capture year to year variation in rainfall. Similar results were found in Small *et al.* [1999] where overestimations in RegCM's annual rainfall led to overestimations in interannual variability for semi-arid regions of central Asia. Likewise, the coefficient of variation, C_v, which measures the dimensionless dispersion of a distribution is, as expected, significantly higher for NCEP at 0.77 versus 0.32 for CRU. In fact, all simulations have coefficients of variation approximately between 0.7 and 0.8 (Table 4.3). These quantities indicate that using the mean alone to describe model performance is insufficient thus, the interannual variability of the model's rainfall is of particular importance. These wildly varying annual totals can also be seen in Figure 4-10 where RegCM3 (NCEP shown) simulates the correct cycle of wet and dry years compared to observations but overestimates the magnitude of above average rainfall years. Also noticeable in Figure 4-10a, is the muted variability of CRU when compared to satellite measurements of rainfall such as GPCP. Consequently, GPCP's standard deviation is 81 mm compared to CRU's 33 mm (Table 4.3). Although it is important to note the coarse resolution of GPCP (2.5° x 2.5°), NCEP variability is still significantly larger than GPCP as well.

By forcing RegCM3 with ERA40 boundary conditions, interannual variability is reduced in RegCM3 simulations. This reduction is better seen in Figure 4-11 which shows model results plotted against observations (CRU & WMO) with the bias, root mean square error (rmse), and the slope of the best fit line, M, displayed. The model's bias describes how well it can reproduce observed mean conditions. The root mean square error (rmse) provides an overall error of model simulations and hence better reflects how well the model reproduces year to year variations in rainfall. Since the rmse includes the bias within the statistic, an improvement to the bias usually results in an improvement to the rmse. The slope is defined as the slope of the best fit line of model output versus observations. A slope greater than one represents model results that overpredict yearly variability while a slope less than one represents an underestimation in interannual variability. Thus, an improvement to the bias, rmse, and slope indicates a model that can more accurately predict mean observational conditions as well as interannual variations in these observations.

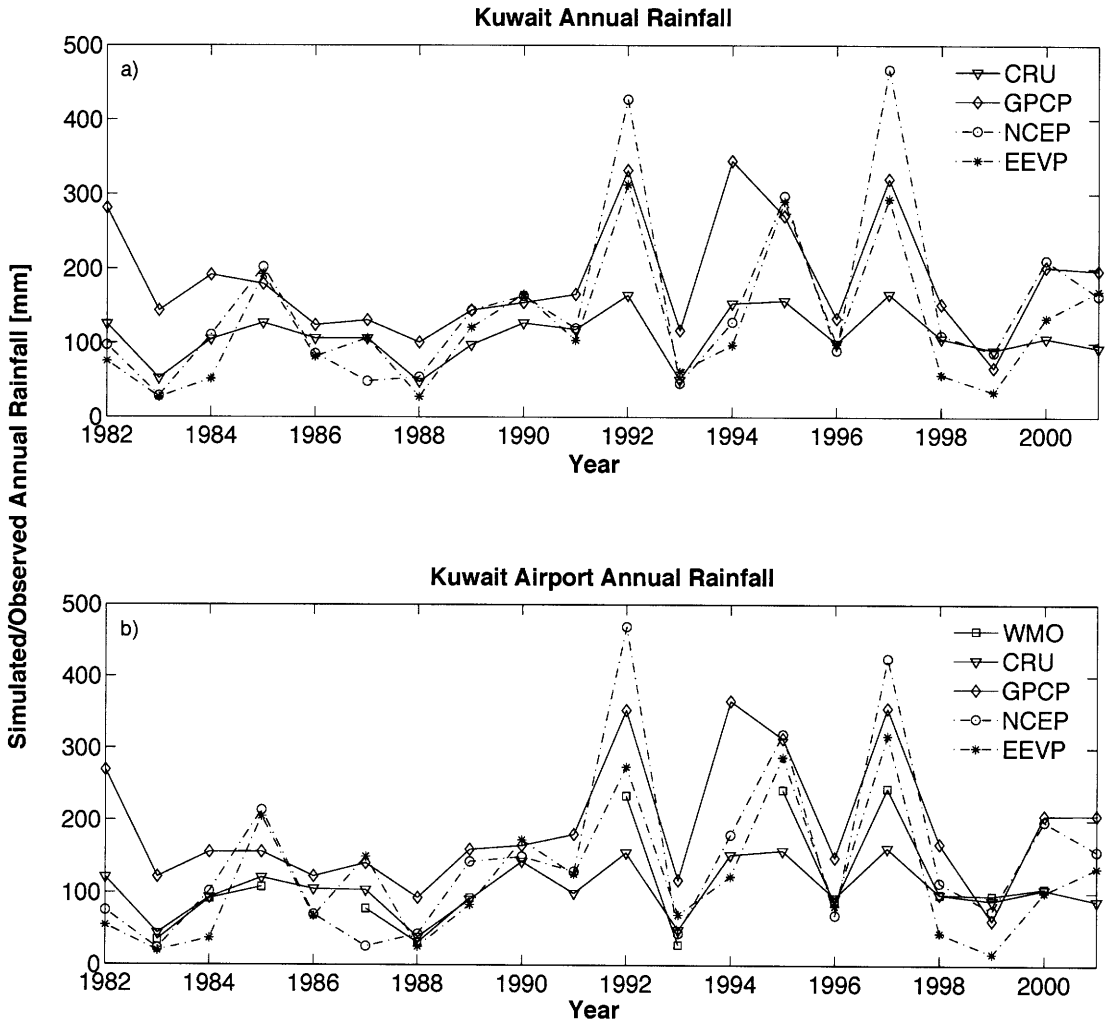

Figure 4-10: Time series (1982-2002) of annual rainfall (mm) for a) country of Kuwait including CRU, GPCP observations, NCEP simulation, and EEVP simulation and b) Kuwait City for same datasets plus WMO airport rain gauge

As seen in Figure 4-11a, NCEP exhibits the highest rmse of 102.7 mm per year. Combined with a slope of 2.6, this simulation clearly does poorest in describing year to year variations in Kuwait rainfall. In fact, in wetter years (those with observations greater than 110mm) NCEP's slope is significantly larger than 2.6. By introducing ERA40 LBC's, the rmse is reduced by 20 mm per year (82.7 mm per year) and the slope is reduced to 2.3. Moreover, ECMW simulations are wetter for years in which NCEP is drier than CRU (see Figure 4-11a & 4-11b). Conversely, ECMW simulates drier years for those in which NCEP is significantly wetter than CRU. Both improvements contribute to a reduction in yearly standard deviations by 15%. Therefore, ECMW better captures year to year variations in Kuwait rainfall.

Comparison to WMO

Due to the large discrepancy in CRU & GPCP values, a comparison is made between Kuwait International Airport's (Kuwait City) rain gauge data and the closest corresponding gridbox in observations and model output. Looking at WMO comparisons (Figure 4-11d), NCEP performs somewhat better at Kuwait City with a rmse of 92.7 mm per year and a slope of 1.9. However, with a yearly standard deviation of 147 mm, NCEP's value is still two times that of WMO. The improvement in rmse and slope is most likely due to the larger variability in the WMO rainfall record. More specifically, WMO has a value of 74 mm which is nearly double that of CRU, thus providing more evidence that CRU values may in fact be smoothed. For example, Figure 4-10b shows that CRU's annual rainfall for Kuwait City is significantly less than that reported by WMO in relatively wet years (e.g. 1992, 1995, & 1997). Moreover, as expected, WMO exhibits a larger C_v at 0.66 than CRU (0.40). As discussed in Chapter 2, techniques used to construct the CRU dataset explain these discrepancies between WMO and CRU. In any event, ECMW performs significantly better with a bias lower by nearly 20 mm per year and a rmse of only 59.6 mm per year. The slope of the best fit line is much closer to unity at 1.4, thus capturing year to year variations in Kuwait City rainfall better than NCEP. This improvement is further seen in the standard deviation of ECMW which is 25% smaller than NCEP (see Table 4.3). It is believed that ECMW's smaller totals in extreme rainfall events contributes most to this improvement.

For instance, in 1997, NCEP predicts nearly 425 mm of rainfall, while for the same year, ECMW only simulates 340 mm, an amount which is nearly 20% less. Thus, with a smaller bias, nearly a 40% reduction in rmse, and a slope closer to unity, ECMW more accurately simulates the rainfall distribution of Kuwait City.

4.4.3 Effects of Sub-cloud Layer Evaporation

As discussed prior, RegCM3 forced with either NCEP or ECMWF boundary conditions significantly overestimates Kuwait's rainfall (Figure 4-7). This wet bias can also be seen in Table 4.4 where an overestimation in Kuwait annual rainfall by 44 and 38 mm occurs, respectively. Although using ERA40 boundary conditions reduces the interannual variability of the model, a large wet bias still exists over Kuwait. By improving the large scale rainfall evaporation rate coefficient as well as introducing sub-cloud layer rainfall evaporation in the convection scheme, a significant reduction in annual rainfall occurs (Figure 4-9c). It is important to note that although the same daily rainfall events occur in Kuwait for both ECMW and EEVP, the magnitude of the rainfall associated with any of these events is significantly reduced in EEVP. Additionally, results indicate that using dynamic evaporation does not markedly modify the spatial distribution of rainfall across the entire domain (see Figure 4-6d). Further work completed compared ECMW & EEVP vertical profiles of specific humidity and temperature. Minimal differences were observed (on the order of 0.01 $g\ kg^{-1}$ & °C). These findings demonstrate that model dynamics are not significantly altered by changes made to RegCM3. Figure 4-9c displays the actual difference (in mm) of rainfall that is evaporated from ECMW in the EEVP simulation. Encouragingly, areas in the domain that RegCM3 significantly overestimates precipitation are the same areas where most precipitation evaporates (compare Figures 4-7b and 4-9c). For example, over the coastlines of the Black & Caspian Seas and the Zagros Mountains where rainfall is significantly overestimated, nearly 500 mm of rainfall evaporates in EEVP. In addition, note the large amount of rainfall that has evaporated over the Arabian Peninsula and Persian Gulf coast where once a significant wet bias occurred in the model (Figure 4-7). As a result, moving further south in the domain to the lands of the hot, arid Syrian & Arabian Deserts, an in-

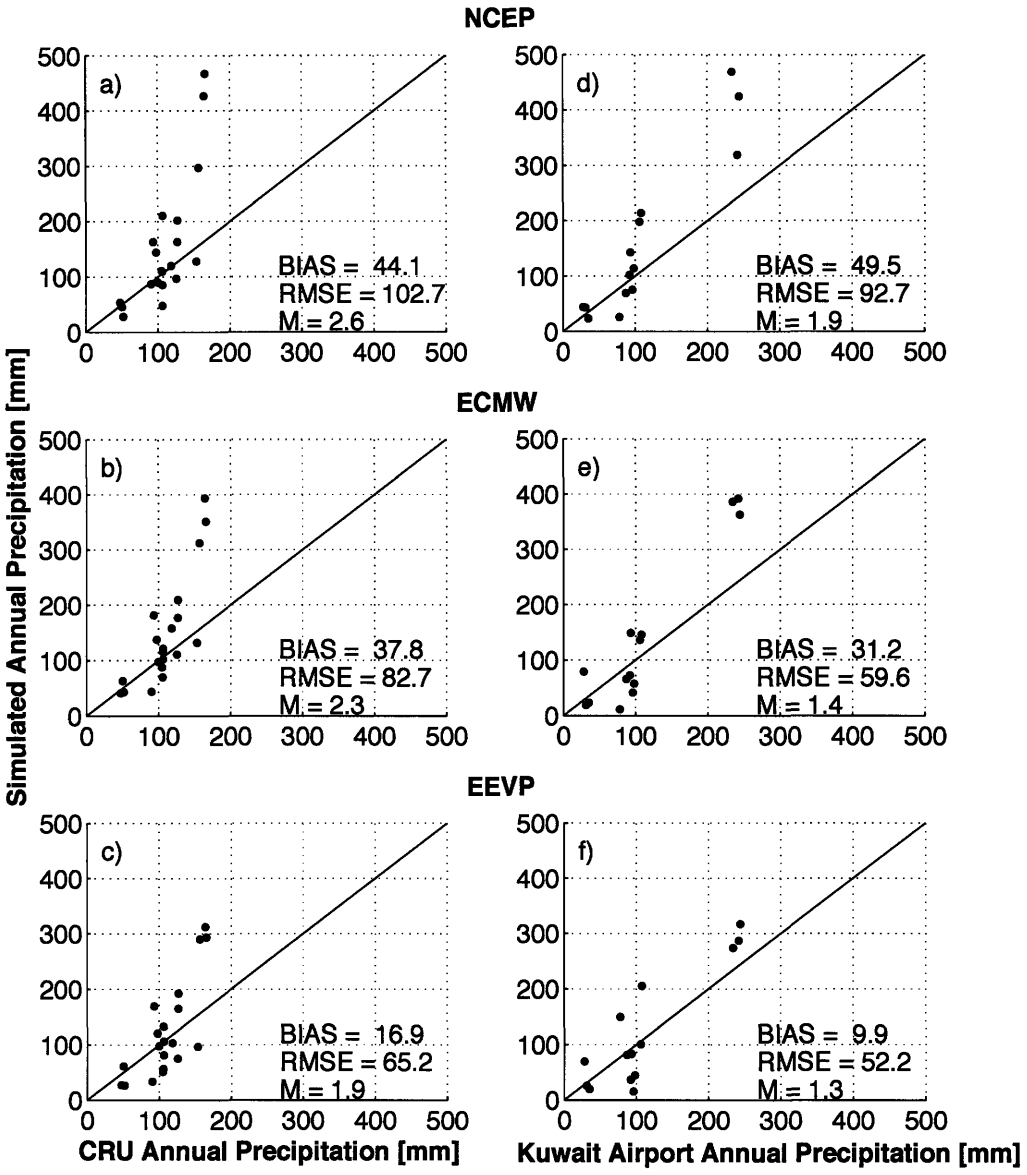

Figure 4-11: For country of Kuwait, a scatter plot of CRU observations versus simulated annual rainfall in a) NCEP b) ECMW and c) EEVP simulation. Also, scatter plot of annual rainfall from WMO Kuwait (City) Airport rain gauge data versus simulations d) NCEP e) ECMW and f) EEVP. Also listed are summary statistics (bias, rmse, M) for each simulation compared to observations. Note that comparisons between WMO and simulations are for 14 years between 1982-2002, those which WMO had a complete rainfall record.

crease in the percentage of total rainfall that evaporates is clearly visible (see Figure 4-9d). For example, in parts of Saudi Arabia more than a third of the total rainfall simulated by RegCM3 in earlier simulations evaporates in EEVP. Therefore, by incorporating this new evaporation scheme, reductions in annual rainfall totals are clearly noticeable.

Comparison to CRU

As seen in Figure 4-11a & 4-11b, both NCEP and ECMW simulations contain large biases of 44.1 and 37.8 mm per year. With our improvements to evaporation in the model, RegCM3's bias is reduced by 21 mm (or 16%) to 126 mm per year. More specifically, in the five years in which ECMW overestimates CRU annual rainfall by the largest amounts, EEVP provides significant reductions in yearly totals. This trend is clearly seen in Figure 4-10a. For example, in the wet years of 1992, 1997, and 2000, EEVP values fall much closer to CRU or GPCP observations. As a result, EEVP contains a bias of only 16.9 mm compared to CRU observations. Also encouraging, this improved evaporation scheme does not drastically reduce dry years (annual rainfall less than 50 mm); only twice do EEVP values fall significantly below observations or other simulations. Additionally, the yearly standard deviation of EEVP (88 mm) is 13% lower than that of ECMW (101 mm). As a result, an improvement is also made to the rmse and slope (see Figure 4-11c). In short, EEVP's smaller bias suggests it is able to produce mean observational values better than NCEP or ECMW. In addition, EEVP's 20% reduction in rmse to 65.2 mm per year suggests that this simulation best represents the year to year variation in Kuwait rainfall. Lastly, from Figure 4-11c it is also noticeable that EEVP's scatter of points lies closest to the one-to-one line of all simulations, or rather, has a slope closest to unity resulting in the most accurate simulation of interannual variability amongst simulations. Therefore, EEVP performs best in simulating the overall hydroclimatology of Kuwait.

Comparison to WMO

Since large differences occur in annual rainfall totals between GPCP & CRU, WMO data is also used in comparing simulations' yearly means. The closest gridbox to Kuwait City Airport in RegCM3 simulations is compared to airport rain gauge data (WMO). From Figure

4-11e & 4-11f, one can see that RegCM3 forced with ERA40 boundary conditions performs better against WMO than against CRU. That is, both RegCM3 simulations (ECMW & EEVP) contain smaller biases, rmse, and slopes for the comparison at the airport (see Table 4.4). This is due mostly to rain gauge values that are larger than CRU measurements for this locale. Nevertheless, apparent in Figure 4-11e, ECMW still contains a large bias of 31.2 mm per year at the airport. The wet bias is mostly caused by RegCM3's difficulty in accurately capturing heavy rainfall years. For example, the wettest three years in WMO are substantially overestimated in the ECMW simulation (Figure 4-11e). By including the modified SUBEX and new convective evaporation schemes, EEVP dramatically decreases total rainfall in each of these wet years (Figure 4-11f). Moreover, four out of the five wettest years simulated in ECMW have a significant reduction in total rainfall in EEVP. This decrease leads to a large reduction in the bias to 9.9 mm per year. Now, simulations are within 9% of observations. Lastly, with modifications made to RegCM3's precipitation schemes, gains in the rmse, slope, and interannual variability are made. For example, EEVP exhibits the lowest rmse (52.2 mm per year) and slope, M, of 1.3 (Table 4.4). As a result, it is clearly visible in Figure 4-11f that EEVP's scatter of points also lies closest to the one-to-one line of all simulations performed. Thus, compared to NCEP & ECMW, EEVP does significantly better in predicting not only Kuwait's annual rainfall but also the annual variation in rainfall.

	Versus CRU			Versus WMO		
	Bias [mm]	RMSE [mm]	M	Bias [mm]	RMSE [mm]	M
CRU	—	—	—	-12.2	39.2	0.51
NCEP	44.1	102.7	2.6	49.5	92.7	1.9
ECMW	37.8	82.7	2.3	31.2	59.6	1.4
EEVP	16.9	65.2	1.9	9.9	52.2	1.3

Table 4.4: Summary statistics for country of Kuwait (simulations versus CRU) and Kuwait City International Airport (versus WMO.) Bias in mm, root mean square error (RMSE) in mm, and slope of the best fit like (M) are presented. Values provided are for the period of 1982-2002 when observations were available from airport (14 years.)

Chapter 5

Conclusions and Future Work

5.1 Summary of Data Analysis

By compiling multiple datasets, basic characteristics and statistics of Kuwait's rainfall are presented. As mentioned prior, discrepancies between CRU, GPCP, and WMO datasets arise from averaging techniques used in creating both CRU and GPCP data. Nevertheless, annual rainfall totals vary from 112 mm (CRU) to 188 mm (GPCP) for the country. In addition, all three datasets show the seasonal cycle of rainfall beginning in November, peaking in both January and March, and subsiding by April. Moreover, yearly standard deviations range from 39 mm (CRU) to 72 mm (GPCP) while small interdecadal variability is observed.

Interannual variability of Kuwait rainfall is weakly influenced by both tropical (ENSO) and mid-latitude (European rainfall) atmospheric features. Since Kuwait is located in the transitional zone between the tropics and mid-latitudes, rainfall in the country is expected to be connected with both tropical climates as well as mid-latitude climates. Here it is found that within the past twenty-five years, Kuwait annual rainfall anomalies are significantly correlated with the Southern Oscillation or El Niño phenomenon. The correlation explains 16% (CRU) or 23% (GPCP) of annual rainfall variability in Kuwait. Likewise, significant spatial correlations are found between Kuwait's rainfall and rainfall over Europe and the Mediterranean region. More specifically, Kuwait's annual rainfall (November through April) is found to be negatively correlated with corresponding Eurasian rainfall

totals. On the other hand, regions of the Mediterranean, and northern Africa are found to have positive correlation with Kuwait's annual rainfall totals. In addition, seasonal variability of the country's rainfall can be explained by the north-south migration of the dominant storm track over the region. That is, a positive correlation with precipitation over the eastern Mediterranean in January shifts further south toward the Red Sea by February before moving north again towards Israel and Syria by March. Although most relationships presented here are statistically significant, they are insufficient for forecasting Kuwait rainfall accurately.

5.2 Summary of Modeling Research

By implementing and improving a simple, yet physically based, sub-cloud layer evaporation scheme, RegCM3's rainfall performance over a semi-arid region has been greatly improved. More specifically, by incorporating dynamic evaporation, the model shows a strong response to rainfall evaporation in sub-cloud layers. As a result, mean model results are now substantially closer to observational datasets. For example, newest model simulations are now within 15% of CRU observations for Kuwait's mean annual rainfall as seen in Figure 5-1. Furthermore, model biases have dropped from nearly 45 mm to 16 mm per year. This improvement is noted all along the Arabian Peninsula where previously a large wet bias in rainfall was simulated by RegCM3 (compare Figure 4-7b to Figure 5-1a and Figure 4-7d to 5-1b). Therefore, it is confirmed that sub-cloud layer evaporation is indeed an important physical process in simulating the mean hydroclimatology of arid regions.

In addition to strides made in annual rainfall totals, simulations of year to year fluctuations in Kuwait rainfall have also been substantially improved. By implementing ERA40 boundary conditions and incorporating dynamic evaporation scheme, interannual variability as well as root mean square errors are significantly reduced. More specifically, a 36% reduction in rmse and 25% reduction in yearly standard deviations occur between NCEP and EEVP. Furthermore, incorporating dynamic evaporation (EEVP) reduces the rmse for Kuwait an additional 17.5 mm per year. Thus, it is shown that along with ERA40 boundary conditions, including sub-cloud layer evaporation in RegCM3 helps improve the accuracy

of simulating the interannual variability of rainfall in semi-arid climates. Encouragingly, rainfall totals now consistently fall in between CRU rain gauge data and GPCP satellite measurements, (Figure 4-10). For example, as shown in Figure 4-10b, EEVP totals lie between WMO & GPCP in most years, particularly the wet years of 1992, 1995, & 1997. Although values now lie closer to these observational datasets, the inaccuracy of RegCM3 in capturing the interannual variability of rainfall is one area still in need of improvement.

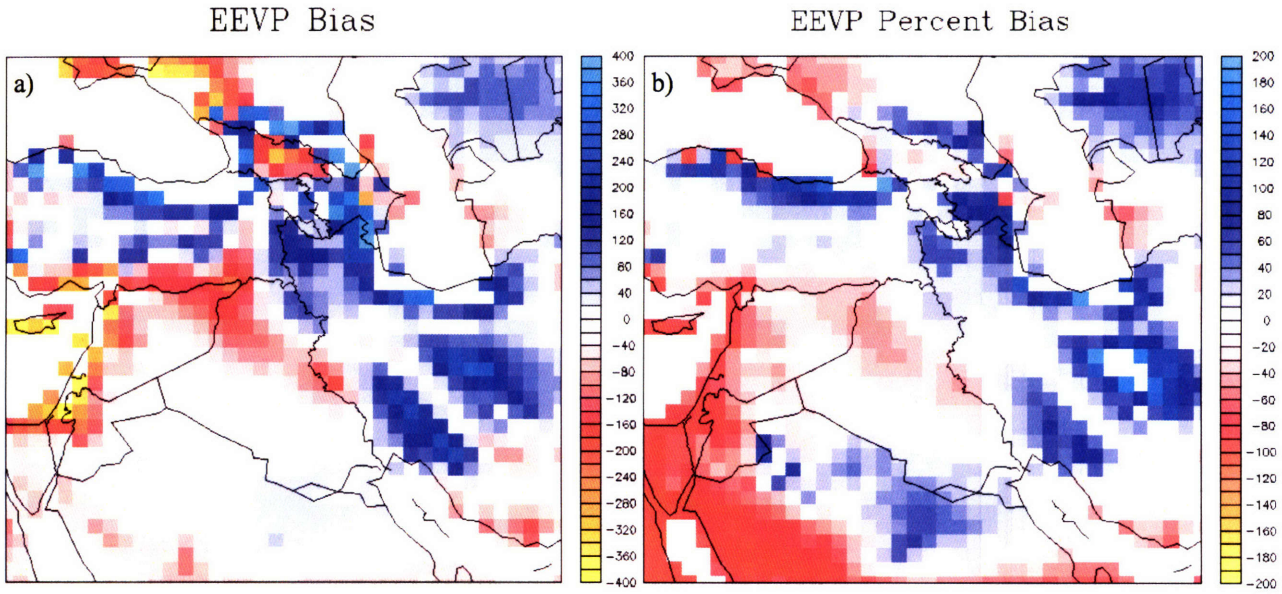

Figure 5-1: Annual precipitation differences between CRU observations and EEVP simulations in a) total difference (mm) and b) percent of total CRU observations.

5.3 Conclusions & Future Work

The combined analysis presented on the hydroclimatology of Kuwait offers a comprehensive and concise description of the country's rainfall at both the seasonal and interannual timescales. Understanding more of the features that dictate variability at these timescales may allow for the possibility of predicting future variability of Kuwait rainfall. For example, if confirmed that anthropogenic forcings do indeed cause an increase in both El Niño strength and frequency, then understanding the relationship between ENSO and Kuwait rainfall becomes particularly useful in forecasting changes to the country's rainfall.

In addition, the modified version of RegCM3 presented can now be used to better sim-

ulate natural climate variability across arid and semi-arid climates. As a result, this tool could be used to predict more accurately changes in rainfall patterns induced by anthropogenic activity in such regions. Therefore, a number of experiments could be performed in the sensitivity analysis of Kuwait's environment-climate feedback. For example, the ability to better predict rainfall patterns leads to the ability to better model vegetation dynamics as well as other land surface processes. Since vegetation and land surface physics play a vital role in the biosphere-atmosphere feedback, these findings should help advance the understanding of this non-linear, dynamic coupling in semi-arid climates.

Lastly, future work includes revising the existing formulation of rainfall evaporation. An examination of the original assumption that evaporation is driven mainly by relative humidity will be performed. Such a formulation may be incomplete since it does not explicitly account for the absolute vapor pressure deficit (or specific humidity) for any given climate but rather is driven by the relative humidity deficit. For example, total rainfall evaporation over arid regions will differ from those over mid-latitude regions due to the strong non-linear dependence of the saturation vapor pressure on temperature (the Clausius Clapeyron effect). As a result, an arid climate's air mass has a larger saturation vapor pressure than a mid-latitude climate. Therefore, its vapor pressure deficit will be larger even given the two regions have the same relative humidity. Thus, in this modified representation, a specific location's saturation vapor pressure (or specific humidity) is explicitly accounted for in deriving rainfall evaporation. Therefore, a more robust representation of subcloud evaporation across different climates would be presented. Results for this new formulation will be documented in the near future.

Appendix A

BATS1e Formulations and Tables

Relevant equations and parameters used in BATS1e are listed below. All formulations are derived from the work of Thom and Oliver [1977], Dickinson *et al.* [1993], and Winter [2006].

Albedo calculations:

Albedo, A_{LBG} can be represented mathematically as:

$$A_{LBG} = A_{LBGO} + \Delta\alpha_g(S_{sw}) \tag{A.1}$$

where A_{LBGO} is the albedo for a saturated soil and $\Delta\alpha_g(S_{sw})$ is a function of the surface soil water content S_{sw} and upper soil layer depth, which gives the increase of albedo due to the dryness of surface soil [Dickinson *et al.*, 1993].

Surface Drag Coefficients:

The drag coefficient, C_D, is given by the drag coefficient for neutral stability, C_{DN}, and the surface bulk Richardson number, Ri_B [Dickinson *et al.*, 1993]:

$$\begin{aligned} C_D &= C_{DN}(1 + 24.5(-C_{DN}Ri_B)^{1/2}) && Ri_B < 0 \\ &= C_{DN}/(1 + 11.5Ri_B) && Ri_B > 0 \end{aligned} \tag{A.2}$$

with C_{DN} calculated from mixing-length theory as follows:

$$C_{DN} = \left[\frac{k}{ln(z_1/z_0)}\right]^2 \tag{A.3}$$

where k is the von Karman constant, z_0 is the roughness length, and z_1 is the height of the lowest model level [Dickinson *et al.*, 1993].

Plant Water expressions:

Implemented in combination with the drip formulae of Massman [1980], interception is calculated as:

$$\tilde{L}_w = \left(\frac{W_{dew}}{W_{DMAX}}\right)^{2/3} \tag{A.4}$$

where, $\tilde{L}_w$ is the fractional area of leaves covered by water, W_{dew} is the total water intercepted by the canopy, and W_{DMAX} is the maximum amount of water the canopy can hold.

It is important to note that in BATS, interception encourages evaporation from wet leaf surfaces while suppressing transpiration from these leaves [Dickinson *et al.*, 1993]. Root resistance follows the work of Federer [1979], Hillel [1980], and Molz [1981]. Following the methodology of Jarvis [1976] and Hinckley *et al.* [1978], specific environmental variables, [i.e. solar radiation, temperature, soil moisture, and vapor pressure deficit] are weighted and combined to find stomatal resistance, r_s. Ultimately, this process is similar in manner as the work presented by Monteith [Thom and Oliver, 1977] to calculate transpiration [Dickinson *et al.*, 1993].

$$r_s = r_{smin} \times R_f \times S_f \times M_f \times V_f \tag{A.5}$$

where r_{smin} is the minimum stomatal resistance, R_f is the dependence of r_s on solar radiation, S_f is the seasonal temperature factor, M_f is a function of soil moisture and root uptake of water, and V_f gives the dependence of r_s on the vapor pressure deficit [Dickinson *et al.*, 1993].

Transpiration formulation:

Transpiration, E_{tr}, is expressed as:

$$E_{tr} = \delta(E_f^{WET}) L_d \left(\frac{r_{la}}{r_{la} + r_s} \right) E_f^{WET} \tag{A.6}$$

where r_{la} is the resistance for heat and water vapor flux, E_f^{WET} is the evaporation rate of water from leaves and stems per unit wetted area, L_d is the fraction of foliage allowed to transpire, and δ is a step function that is 1 (0) when the argument E_f^{WET} is positive (negative) [Dickinson *et al.*, 1993].

Soil Temperature equation:

One of the more important surface variables, surface soil temperature, T_{g1}, is expressed as:

$$C\Delta t \frac{\partial T_{g1}}{\partial t} + 2AT_{g1} = B \tag{A.7}$$

Here, A is a function of the diurnal frequency, B is a term proportional to net surface heating, C is dependent on the thermal inertia of freezing, and Δt is the timestep in seconds.

The soil temperature expression is modeled after the force restore method of Deardorff [1978], and is explicitly documented in Dickinson and Sellers [1988]. Following the work of Maykut and Untersteiner [1971] and Semtner Jr. [1976], a simpler scheme for sea ice is used and basically models a constant heat conduction from the ocean.

Infiltration and Runoff expressions:

Infiltration is dictated by the diffusivity, D, which is mathematically expressed as:

$$D = K_{wo}\phi_o B s^{B+2} \tag{A.8}$$

where K_{wo} is the hydraulic conductivity, s is the volume of water divided by the volume of water at saturation, B is the Clapp and Hornberger [1978] exponent, and ϕ_o is the minimum soil suction [Dickinson *et al.*, 1993]. At larger length scales, infiltration can be influenced by the subsoil drainage [Dickinson *et al.*, 1993].

Runoff R_s is formulated by:

$$\begin{aligned} R_s &= (\rho_w/\rho_{wsat})^4 G && T_{g1} \geq 0^o C \\ &= (\rho_w/\rho_{wsat}) G && T_{g1} < 0^o C \end{aligned} \tag{A.9}$$

Here, the soil water density, ρ_w, is weighted toward the top layer, ρ_{wsat} is the saturated soil water density, and G is the net water applied to the surface [Dickinson *et al.*, 1993].

Parameter	Land Cover/Vegetation Type																			
	1	2	3	4	5	6	7	8	9	10	11	12	13	14	15	16	17	18	19	20
Max fractional vegetation cover	0.85	0.80	0.80	0.80	0.80	0.90	0.80	0.00	0.60	0.80	0.35	0.00	0.80	0.00	0.00	0.80	0.80	0.80	0.80	0.80
Difference between max fractional vegetation cover and cover at 269 K	0.6	0.1	0.1	0.3	0.5	0.3	0.0	0.2	0.6	0.1	0.0	0.4	0.0	0.0	0.2	0.3	0.2	0.4	0.4	
Roughness length (m)	0.08	0.05	1.00	1.00	0.80	2.00	0.10	0.05	0.04	0.06	0.10	0.01	0.03	0.0004	0.0004	0.10	0.10	0.80	0.3	0.3
Displacement height (m)	0.0	0.0	9.0	9.0	0.0	18.0	0.0	0.0	0.0	0.0	0.0	0.0	0.0	0.0	0.0	0.0	0.0	0.0	0.0	0.0
Min stomatal resistence (s/m)	45	60	80	80	120	60	60	200	80	45	150	200	45	200	200	80	120	100	120	120
Max Leaf Area Index	6	2	6	6	6	6	6	0	6	6	6	0	6	0	0	6	6	6	6	6
Min Leaf Area Index	0.5	0.5	5	1	1	5	0.5	0	0.5	0.5	0.5	0	0.5	0	0	5	1	3	0.5	0.5
Stem (& dead matter) area index)	0.5	4.0	2.0	2.0	2.0	2.0	2.0	0.5	0.5	2.0	2.0	2.0	2.0	2.0	2.0	2.0	2.0	2.0	2.0	2.0
Inverse square root of leaf dimension ($m^{-1/2}$)	10	5	5	5	5	5	5	5	5	5	5	5	5	5	5	5	5	5	5	5
Light sensitivity factor (m^2 W^{-1})	0.02	0.02	0.06	0.06	0.06	0.06	0.02	0.02	0.02	0.02	0.02	0.02	0.02	0.02	0.02	0.02	0.02	0.06	0.02	0.02
Upper soil layer depth (mm)	100	100	100	100	100	100	100	100	100	100	100	100	100	100	100	100	100	100	100	100
Root zone soil layer depth (mm)	1000	1000	1500	1500	2000	1500	1000	1000	1000	1000	1000	1000	1000	1000	1000	1000	1000	2000	2000	2000
Depth of total soil (mm)	3000	3000	3000	3000	3000	3000	3000	3000	3000	3000	3000	3000	3000	3000	3000	3000	3000	3000	3000	3000
Soil texture type	6	6	6	6	7	8	6	3	6	6	5	12	6	6	6	6	5	6	6	0
Soil color type	5	3	4	4	4	4	4	1	3	3	2	1	5	5	5	4	3	4	4	0
Vegetation albedo for wavelengths < 0.7 μ m	0.10	0.10	0.05	0.05	0.08	0.04	0.08	0.20	0.10	0.08	0.17	0.80	0.06	0.07	0.07	0.05	0.08	0.06	0.06	0.06
Vegetation albedo for wavelengths > 0.7 μ m	0.30	0.30	0.23	0.23	0.28	0.20	0.30	0.40	0.30	0.28	0.34	0.60	0.18	0.20	0.20	0.23	0.28	0.24	0.18	0.18

Table A.1: Parameters for BATS1e [Elguindi *et al.*, 2004].

Bibliography

ADLER, R., G. HUFFMAN, A. CHANG, R. FERRARO, P. XIE, J. JANOWIAK, B. RUDOLF, U. SCHNEIDER, S. CURTIS, D. BOLVIN, A. GRUBER, J. SUSSKIND, P. ARKIN and E. NELKIN. The Version 2 Global Precipitation Climatology Project (GPCP) Monthly Precipitation Analysis (1979-Present). *Journal of Hydrometeorology*, 4:pages 1147–1167 [2003].

AL KULAIB, A. *The Climate of Kuwait*. Al Ressala P. Press [1984].

AL-RASHED, M. F. and M. M. SHERIF. Water Resources in the GCC Countries. *Water Resources Management*, 14:pages 59–75 [2000].

ANTHES, R. A cumulus parameterization scheme utilizing a one-dimensional cloud model. *Monthly Weather Review*, 105(3):pages 270–286 [1977].

ANTHES, R., E. HSIE and Y.-H. KUO. Description of the Penn State / NCAR Mesoscale Model version 4 (MM4). Technical Note TN-282+STR, National Center for Atmospheric Research [1987].

ARAKAWA, A. and W. H. SCHUBERT. Interaction of a cumulus cloud ensemble with large-scale environment, part 1. *Journal of Atmospheric Sciences*, 31(3):pages 674–701 [1974].

BEHENG, K. A parameterization of warm cloud microphysical conversion processes. *Atmospheric Research*, 33(1-4):pages 193–206 [1994].

BRIEGLEB, B. P. Delta-eddington approximation for solar radiation in the NCAR community climate model. *Journal of Geophysical Research*, 97(D7):pages 7603–7612 [1992].

CLAPP, R. and G. HORNBERGER. Empirical equations for some soil hydraulic properties. *Water Resources Research*, 14(4):pages 601–604 [1978].

COAKLEY JR., J. A., R. D. CESS and F. B. YUREVICH. The effect of tropospheric aerosols on the Earth's radiation budget: A parameterization for climate models. *Journal of Atmospheric Sciences*, 40(1):pages 116–138 [1983].

CULLEN, H., A. KAPLAN, P. ARKIN and P. B. DEMENOCAL. Impact of the North Atlantic Oscillation on Middle Eastern Climate and Streamflow. *Climatic Change*, 55:pages 315–338 [2002].

DAVIES, H. and R. TURNER. Updating prediction models by dynamical relaxation: An examination of the technique. *Quarterly Journal of the American Meteorological Society*, 103(436):pages 225–245 [1977].

DEARDORFF, J. W. Parameterization of the planetary boundary layer for use in general circulation models. *Monthly Weather Review*, 100(2):pages 93–106 [1972].

—. Efficient prediction of ground surface temperature and moisture, with inclusion of a layer of vegetation. *Journal of Geophysical Research*, 83(C4):pages 1889–1904 [1978].

DICKINSON, R., R. ERRICO, F. GIORGI and G. BATES. A regional climate model for the western United States. *Climate Change*, 15(3):pages 383–422 [1989].

DICKINSON, R., A. HENDERSON-SELLERS and P. KENNEDY. Biosphere Atmosphere Transfer Scheme (BATS) version 1E as coupled to the NCAR Community Climate Model. Tech. rep., National Center for Atmospheric Research [1993].

DICKINSON, R., P. KENNEDY, A. HENDERSON-SELLERS and M. WILSON. Biosphere-Atmosphere Transfer Scheme (BATS). Technical Note TN-275+STR, National Center for Atmospheric Research [1986].

DICKINSON, R. E. and A. SELLERS. Modelling tropical deforestation: A study of GCM land-surface parametrizations. *Quarterly Journal of the Royal Meteorological Society*, 114(480):pages 439–462 [1988].

EBERT, E. E. and J. A. CURRY. A parameterization of ice cloud optical properties for climate models. *Journal of Geophysical Research*, 97(D4):pages 3831–3836 [1992].

EBISUZAKI, W. NCEP/DOE AMIP-II reanalysis, Last Visited - 11 May 2006, http://www.cpc.ncep.noaa.gov/products/wesley/reanalysis2/index.html [2005].

ELGUINDI, N., X. BI, F. GIORGI, B. NAGARAJAN, J. S. PAL and F. SOLMON. *RegCM version 3.0 User's Guide*. International Centre for Theoretical Physics, Trieste, Italy, 1 ed. [2004].

EMANUEL, K. A. A scheme for representing cumulus convection in large-scale models. *Quarterly Journal of the Royal Meteorological Society*, 48(21):pages 2313–2329 [1991].

EUROPEAN CENTRE FOR MEDIUM-RANGE WEATHER FORECASTS. The description of the ECMWF/WCRP level III-A global atmospheric data archive, Last Visited - 11 May 2006, http://www.cgd.ucar.edu/cas/catalog/ecmwf/wcrpi/daily.html [1995].

EVANS, J., R. OGLESBY, K. MAASCH and R. SMITH. Investigation of Middle Eastern climate using a regional climate model. In *13th Symposium on global change and climate variations*. American Meteorological Society [2002].

EVANS, J., R. SMITH and R. OGLESBY. Middle East Climate Simulation and Dominant Precipitation Processes. *International Journal of Climatology*, 24:pages 1671–1694 [2004].

FADLELMAWLA, A. and M. AL-OTAIBI. Analysis of the Water Resources Status in Kuwait. *Water Resources Management*, 19:pages 555–570 [2005].

FEDERER, C. A soil-plant-atmosphere model for transpiration and availability of soil water. *Water Resources Research*, 15(3):pages 555–562 [1979].

FRITSCH, J. and C. CHAPPELL. Numerical prediction of convectively driven mesoscale pressure systems. Part I: Convective parameterizations. *Journal of Atmospheric Sciences*, 37(8):pages 1722–1733 [1980].

GEORGAKAKOS, K. P. and R. L. BRAS. A Hydrologically Useful Station Precipitation Model: 1. Formulation. *Water Resources Research*, 20(11):pages 1585–1597 [1984].

GIORGI, F. Simulation of regional climate using a limited area model nested in a general circulation model. *Journal of Climate*, 3(9):pages 941–963 [1990].

GIORGI, F. and G. BATES. The climatological skill of a regional model over complex terrain. *Monthly Weather Review*, 117(11):pages 2325–2347 [1989].

GIORGI, F. and R. MARINUCCI. Validation of a regional atmospheric model over Europe: Sensitivity of wintertime and summertime simulations to selected physics parametizations and lower boundary condition. *Quarterly Journal of the Royal Meteorological Society*, 117(502):pages 1171–1206 [1991].

GIORGI, F., L. MEARNS, C. SHIELDS and L. MCDANIEL. Regional nested model simulations of present day and 2XCO2 climate over the Central Plains of the U.S. *Climatic Change* [1998].

GIORGI, F. and C. SHIELDS. Tests of precipitation parameterizations available in latest version of NCAR regional climate model (RegCM) over continental United States. *Journal of Geophysical Research*, 104(D6):pages 6353–6375 [1999].

GRELL, G. A. Prognostic evaluation of assumptions used by cumulus parameterizations. *Monthly Weather Review*, 121(3):pages 764–787 [1993].

GRELL, G. A., J. DUDHIA and D. STAUFFER. A description of the fifth-generation Penn State/NCAR Mesoscale Model (MM5). Technical Note TN-398+IA, National Center for Atmospheric Research [1994].

HACK, J. J., B. A. BOVILLE, B. P. BRIEGLEB, J. T. KIEHL, P. J. RASCH and D. L. WILLIAMSON. Description of the NCAR Community Climate Model (CCM2). Technical Note TN-382+STR, National Center for Atmospheric Research [1993].

HILLEL, D. *Application of soil physics*. Academic Press, New York [1980].

HINCKLEY, T., J. LASSOIE and S. RUNNING. Temporal and spatial variations in the water status for forest trees. *Forest Science Monograph*, 20:pages 1–72 [1978].

HOLTSLAG, A., E. DE BRUIN and H. PAN. A high resolution air mass transformation model for short-range weather forecasting. *Monthly Weather Review*, 118:pages 1561–1575 [1990].

HOLTSLAG, A. and C.-H. MOENG. Eddy diffusivity and countergradient transport in the convective atmospheric boundary layer. *Journal of Atmospheric Sciences*, 48(14):pages 1690–1698 [1991].

HSIE, E., R. ANTHES and D. KEYSER. Numerical simulation of frontogenisis in a moist atmosphere. *Journal of Atmospheric Sciences*, 41(17):pages 2581–2594 [1984].

HURRELL, J. W. Decadal Trends in the North Atlantic Oscillation: Regional Temperature and Precipitation. *Science*, 269(5224):pages 676–678 [1995].

JARVIS, P. The interpretation of the variations in leaf water potential and stomatal conductance found in canopies in the field. *Philisophical Transactions of the Royal Society of London. Series B, Biological Sciences*, 273(927):pages 593–610 [1976].

JOSEPH, J., W. WISCOMBE and J. WEINMAN. The Delta-Eddington approximation for radiative flux transfer. *Journal of Atmospheric Sciences*, 33(12):pages 2452–2459 [1976].

KALNAY, E., M. KANAMITSU, R. KISTLER, W. COLLINS, D. DEAVEN, L. GANDIN, M. IREDELL, S. SAHA, G. WHITE, J. WOOLLEN, Y. ZHU, A. LEETMAA, B. REYNOLDS, M. CHELLIAH, W. EBISUZAKI, W. HIGGINS, J. JANOWIAK, K. MO, C. ROPELEWSKI, J. WANG, R. JENNE and D. JOSEPH. The NCEP/NCAR 40-year reanalysis project. *Bulletin of the American Meteorological Society*, 77(3):pages 437–471 [1996].

KIEHL, J., J. HACK, G. BONAN, B. BOVILLE, B. BREIGLEB, D. WILLIAMSON and P. J. RASCH. Description of the NCAR Community Climate Model (CCM3). Technical Note TN-420+STR, National Center for Atmospheric Research [1996].

KUMAR, K. K., B. RAJAGOPALAN, M. HOERLING, G. BATES and M. CANE. Unraveling the Mystery of Indian Monsoon Failure During El Nino. *Science*, 314:pages 115–118 [2006].

KUO, H. Further studies of the parameterization of the influence of cumulus convection on large-scale flow. *Journal of Atmospheric Sciences*, 31(5):pages 1232–1240 [1974].

MASSMAN, W. Water storage on forest foliage: A general model. *Water Resources Research*, 16(1):pages 210–216 [1980].

MAYKUT, G. A. and N. UNTERSTEINER. Some results from a time-dependent thermodynamic model of sea ice. *Journal of Geophysical Research*, 76(6):pages 1550–1576 [1971].

MITCHELL, T. D. and P. D. J. JONES. An improved method of constructing a database of monthly climate observations and associated high-resolution grids. *International Journal of Climatology*, 25(6):pages 693–712 [2005].

MOLZ, F. Model of water transport in the soil-plant system: A review. *Water Resources Research*, 17(5):pages 1245–1260 [1981].

MONTEITH, J. *Vegetation and the atmosphere*, vol. 1-2. Academic Press, London [1976].

MUKHOPADHYAY, A., A. AKBER, E. AL-AWADI and N. BURNEY. Analysis of Freshwater Consumption Pattern in Kuwait and its Implication for Water Management. *Water Resources Development*, 16(4):pages 543–561 [2000].

NEW, M., M. HULME and J. P.D. Representing twentieth century space-time climate variability. Part I: Development of a 1961-90 mean monthly terrestrial climatology. *Journal of Climate*, 12(3):pages 829–856 [1999].

PAL, J., E. SMALL and E. A. B. ELTAHIR. Simulation of regional-scale water and energy budgets: Representation of subgrid cloud and precipitation processes within RegCM. *Journal of Geophysical Research*, 105 [2000].

PAL, J. S. *The role of soil moisture conditions in the occurence of floods and droughts over the Mississippi Basin.* Master's thesis, Massachusetts Institute of Technology [1997].

—. *Modeling the role of soil moisture in North American summer climate.* Ph.D. thesis, Massachusetts Institute of Technology [2001].

PALTRIDGE, G. and C. PLATT. *Radiative processes in meteorology and climatology.* Elsevier Scientific Publishing Company, Amsterdam [1976].

PRICE, C., L. STONE, A. HUPPERT, B. RAJAGOPALAN and P. ALPERT. A possible link between El Nino and precipitation in Israel. *Geophysical Research Letters*, 25(21):pages 3963–3966 [1998].

PRUPPACHER, H. and J. KLETT. *Microphysics of Clouds and Precipitation.* D. Reidel, Boston, Massachusetts [1978].

RAJAGOPALAN, B., U. LALL and M. CANE. Anomalous ENSO occurrences: An alternate view. *Journal of Climate*, 10:pages 2351–2357 [1997].

RAMANATHAN, V. and P. DOWNEY. A nonisothermal emissivity and absorptivity formulation for water vapor. *Journal of Geophysical Research*, 9(D8):pages 8649–8666 [1986].

RAYNER, N. A., E. HORTON, D. PARKER, C. FOLLAND and R. HACKETT. Version 2.2 of the global sea ice and sea surface temperature dataset, 1903-1994. Technical Note 74, Hadley Centre [1996].

REYNOLDS, R. W. An improved in situ and satellite SST analysis for climate. *Journal of Climate*, 15:pages 1609–1625 [2002].

REYNOLDS, R. W., N. A. RAYNER, T. M. SMITH, D. C. STOKES and W. WANG. An improved in situ and satellite SST analysis for climate. *Journal of Climate*, 15(13):pages 1609–1625 [2002].

ROGERS, P. and P. LYDON, eds. *Water in the Arab World: Perspectives and Prognoses.* The Division of Applied Sciences, Harvard University [1994].

ROSENFELD, D. and Y. MINTZ. Evaporation of Rain Falling from Convective Clouds as Derived from Radar Measurements. *Journal of Applied Meteorology*, 27:pages 209–215 [1988].

SELLERS, W. *Physical climatology*. Univeristy of Chicago Press, Chicago [1965].

SEMTNER JR., A. J. A model for the thermodynamic growth of sea ice in numerical investigations of climate. *Journal of Physical Oceanography*, 6(3):pages 379–389 [1976].

SLINGO, A. A GCM parameterization for the shortwave radiative properties of water clouds. *Journal of Atmospheric Sciences*, 46(10):pages 1419–1427 [1989].

SMALL, E., F. GIORGI and L. SLOAN. Regional climate model simulation of precipitation in central Asia : Mean and interannual variability. *Journal of Geophysical Research*, 104(D6):pages 6563–6582 [1999].

SMALL, E. E. and L. SLOAN. Simulating the water balance of the aral sea with a coupled regional climate-lake model. *Journal of Geophysical Research*, 104(D6):pages 6583–6602 [1999].

SUNDQVIST, H., E. BERGE and J. KRISTJANSSON. Condensation and Cloud Parameterization Studies with a Mesoscale Numerical Weather Prediction Model. *Monthly Weather Review*, 117:pages 1641–1657 [1989].

SYED, F., F. GIORGI, J. PAL and M. KING. Effect of remote forcings on the winter precipitation of central southwest Asia Part 1: Observations. *Theoretical and Applied Climatology*, 86:pages 147–160 [2006].

THOM, A. and H. OLIVER. On Penman's equation for estimating regional evaporation. *Quarterly Journal of the Royal Meteorological Society*, 103(436):pages 345–357 [1977].

UNITED STATES GEOLOGICAL SURVEY. Global 30 arc second elevation data (GTOPO30), Last Visited - May 9, 2006, http://edc.usgs.gov/products/elevation/gtopo30/gtopo30.html [1996].

—. Global Land Cover Characterization, Last Visited - 11 May 2006, http://edcsns17.cr.usgs.gov/glcc/ [1997].

UPPALA, S., P. KALLBERG, A. SIMMONS, U. ANDRAE, V. DA COSTA BECHTOLD, M. FIORINO, J. GIBSON, J. HASELER, A. HERNANDEZ, G. KELLY, X. LI, K. ONOGI, S. SAARINEN, N. SOKKA, R. ALLAN, E. ANDERSSON, K. ARPE, M. BALMASEDA, A. BELJAARS, L. VAN DE BERG, J. BIDLOT, N. BORMANN, S. CAIRES, F. CHEVALLIER, A. DETHOF, M. DRAGOSAVAC, M. FISHER, M. FUENTES, S. HAGEMANN, E. HOLM, B. HOSKINS, L. ISAKSEN, P. JANSSEN, R. JENNE, A. MCNALLY, J.-F. MAHFOUF, J.-J. MORCRETTE, N. RAYNER, R. SAUNDERS, P. SIMON, A. STERL, K. TRENBERTH, A. UNTCH, D. VASILJEVIC, P. VITERBO and J. WOOLLEN. The ERA-40 re-analysis. *Quarterly Journal of the Royal Meteorological Society*, 131(612):pages 2961–3012 [2005].

WALTERS, K. R. The Persian Gulf Region : A Climatological Study. Technical Note USAFETAC/TN-88/002, USAF Environmental Technical Applications Center [1988].

WINTER, J. M. *Coupling of Integrated Biosphere Simulator to Regional Climate Model version 3*. Master's thesis, Massachusetts Institute of Technology [2006].

WORDEN, J., D. NOONE and K. BOWMAN. Importance of rain evaporation and continental convection in the tropical water cycle. *Nature*, 445(7127):pages 528–532 [2007].

WUETHRICH, B. El Nino goes critical. *New Scientist*, pages 32–35 [1995].

YIAO, Y. and D. CAYA. An investigation of summer precipitation simulated by the Canadian Regional Climate Model. *Monthly Weather Review*, 134(3):pages 919–932 [2006].

ZENG, X., M. ZHAO and R. DICKINSON. Intercomparison of bulk aerodynamic algorithms for the computation of sea surface fluxes using TOGA coare and TAO data. *Journal of Climate*, 11:pages 2628–2644 [1998].